Cessation of Labrador Sea Convection Triggered by Distinct Fresh and Warm (Sub)Mesoscale Flows

Louis Clément [a], E. Frajka-Williams,[b] N. von Oppeln-Bronikowski,[c] I. Goszczko,[d] and B. de Young[c]

[a] National Oceanography Centre, Southampton, United Kingdom
[b] Universität Hamburg, Hamburg, Germany
[c] Memorial University, St John's, Canada
[d] Institute of Oceanology PAN, Sopot, Poland

ABSTRACT: By ventilating the deep ocean, deep convection in the Labrador Sea plays a crucial role in the climate system. Unfortunately, the mechanisms leading to the cessation of convection and, hence, the mechanisms by which a changing climate might affect deep convection remain unclear. In winter 2020, three autonomous underwater gliders sampled the convective region and both its spatial and temporal boundaries. Both boundaries are characterized by higher subdaily mixed layer depth variability sampled by the gliders than the convective region. At the convection boundaries, buoyant intrusions—including eddies and filaments—instead of atmospheric warming primarily trigger restratification by bringing buoyancy with a comparable contribution from either fresh or warm intrusions. At the edges of these intrusions, submesoscale instabilities, such as symmetric instabilities and mixed layer baroclinic instabilities, seem to contribute to the decay of the intrusions. In winter, enhanced lateral buoyancy gradients are correlated with strong destabilizing surface heat fluxes and alongfront winds. Consequently, winter atmospheric conditions and buoyant intrusions participate in halting convection by triggering restratification while surface fluxes are still destratifying. This study reveals freshwater anomalies in a narrow area offshore of the Labrador Current and near the convective region; this area has received less attention than the more eddy-rich West Greenland Current, but is a potential source of freshwater in closer proximity to the region of deep convection. Freshwater fluxes from the Arctic and Greenland are expected to increase under a changing climate, and our findings suggest that they may play an active role in the restratification of deep convection.

KEYWORDS: Boundary currents; Deep convection; Fronts; Potential vorticity; Eddies; Freshwater

1. Introduction

In the subpolar North Atlantic, the Labrador Sea hosts vigorous winter deep convection (Lazier et al. 2002), a crucial element of our climate system. By ventilating intermediate and deep water masses with mixed layer properties, convection forms Labrador Sea Water (LSW), a cold and freshwater mass that is rich in carbon dioxide and oxygen, and that subsequently fills the deep ocean (Yashayaev et al. 2007). Although recent interannual observations emphasized the role of eastern subpolar basins for the transformation of the lightest water masses (Lozier et al. 2019), the Labrador Sea remains a key driver of the deep ocean ventilation (Rhein et al. 2002; Sabine et al. 2004) and potentially of the multidecadal variability of the Atlantic meridional overturning circulation (Yeager et al. 2021). Understanding the convection life cycle and specifically its cessation remains critical to comprehend the effects of a warming climate on convection, i.e., the effects of a warmer ocean and of enhanced freshwater fluxes (Manabe and Stouffer 1995; Rahmstorf 1995) from Arctic (Proshutinsky et al. 2019) and Greenland (Bamber et al. 2012) origins.

Despite a focus on the onset of convection (Lab Sea Group 1998), sampling and understanding restratification in late winter have been hampered by harsh winter conditions. Another challenge lingers in simulating both large-scale buoyant boundary currents while capturing small-scale transient processes, that contribute to restratification. Accordingly, numerical models coarsely represent the effect of added freshwater on convection in hosing experiments, by evenly distributing freshwater in the subpolar North Atlantic (Vellinga and Wood 2002). Furthermore, climate models and high-resolution models overpredict the spatial extent of deep convection in the Labrador Sea (Heuzé 2017; Koenigk et al. 2021). Capturing submesoscale processes, in particular the frontal circulation found around eddies and filaments, generates a more realistic cessation of deep convection or production of LSW (Tagklis et al. 2020; Pennelly and Myers 2020). These processes host strong ageostrophic vertical velocities that restratify surface boundary layer through vertical buoyancy fluxes from the ocean interior into the mixed layer (ML; Thomas et al. 2008). Consequently, in climate models, one-dimensional vertical parameterization of mixed layer restratification by atmospheric forcing (Large et al. 1994) misses the potential influence of the lateral buoyancy gradient (Fox-Kemper et al. 2008; Mahadevan et al. 2012).

Despite the role of convection in our climate system, the processes that drive restratification and limit the production of LSW remain poorly understood. For example, the relative importance of shallow freshwater and of subsurface warm waters originating in the boundary currents, and that may involve not only mesoscale but also submesoscale flows, are yet to be established.
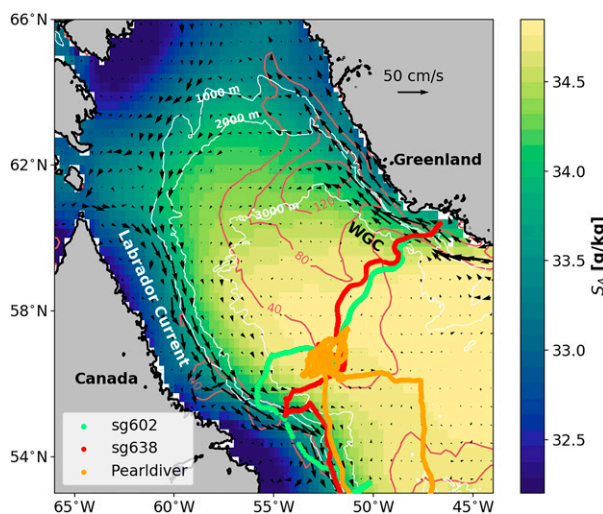

FIG. 1. Mean surface geostrophic current (arrows) and eddy kinetic energy (cm^2 s^{-2}; red contours) over 1993–2020 estimated from the altimeter satellite gridded sea level anomalies. Glider trajectories (colored dots) and sea surface salinity climatology from *World Ocean Atlas* (2005–17). The major surface currents are the West Greenland Current (WGC) and the Labrador Current. Isobaths are added in white.

Cyclonic boundary currents enter the Labrador Sea south of Greenland as the West Greenland Current (WGC; Fig. 1) bringing shallow cold and fresh waters of Arctic and Greenland origins over the shelves (Lazier 1973; Cuny et al. 2002). Below and offshore the WGC, the Irminger Current brings subsurface warm and salty waters of North Atlantic origin over continental slopes. Along western Greenland, additional freshwater from the Greenland ice sheet melting joins the shallow currents. Then, the WGC flows north and part of it circulates southwestward while receiving more Arctic waters that flows out of Baffin Bay. The current then flows along the eastern coast of Canada and Hudson Bay, where it receives more freshwater (Florindo-López et al. 2020), to form the Labrador Current.

Initially, baroclinic instabilities of convective patches were used to explain restratification without invoking buoyant boundary currents (Visbeck et al. 1996; Jones and Marshall 1997). Subsequently and based on observed warm eddies (Lilly et al. 2003), boundary currents were thought to bring buoyancy through lateral eddy fluxes and, thus, simulations controlled their restratification via heat only (Katsman et al. 2004; Spall 2004; Chanut et al. 2008).

In addition, freshwater fluxes were hypothesized to contribute to the seasonal cessation of convection, along with their long-term effect on the cessation of convection (Manabe and Stouffer 1995). In subpolar cool oceans, freshwater fluxes primarily affect density (Aagaard and Carmack 1989) such as during Great Salinity Anomalies (GSAs), for example, in the 1970s (Dickson et al. 1988). Although freshwater eddies enter the central Labrador Sea (Hátún et al. 2007), their net freshwater contribution to restratification or to GSAs remains speculative and uncertain (Lazier 1980; Straneo 2006a). Partly

contributing to this uncertainty are inaccurate estimations of surface freshwater fluxes and an opposing winter positive salt flux into the mixed layer. Despite these limitations, Straneo (2006a) observed in May (just after restratification) a faster shallow freshening than accounted for by atmospheric fluxes, underlying the key role of lateral freshwater transport. Schmidt and Send (2007) also noticed a freshening of the Labrador Sea interior starting in April only, i.e., without winter freshening, although they could not determine the origin, whether eastern (WGC) or western (from the Labrador Current), by studying the currents' seasonality.

Based on the observed enhanced winter eddy kinetic energy along the western coast of Greenland, many studies have focused on the large eddies generated off Greenland (in the WGC) to explain the seasonal buoyancy export into the interior's Labrador Sea. In contrast, Brandt et al. (2004) underlined the role of the Labrador Current in eddy generation, potentially through baroclinic instabilities (Eden and Böning 2002). In addition, only high-resolution simulations [at least 1/10°, 9 km; Zhang et al. (2021)] capture shelf-basin freshwater exchanges (Böning et al. 2016; Dukhovskoy et al. 2019; Swingedouw et al. 2022) from the Labrador Current (McGeehan and Maslowski 2011; Pennelly et al. 2019) while lower-resolution models revealed weak exchanges (Myers 2005).

Despite extensive studies of mesoscale variability in the Labrador Sea, the contribution of submesoscale processes to restratification remains elusive in the deep convective regions. Submesoscale processes, such as symmetric instabilities and mixed layer baroclinic instabilities, with small temporal (from hours to days) and spatial scales (0.1–10 km) have the potential to restratify the surface mixed layer. For example, such restratification was disclosed in the open-ocean North Atlantic (Thompson et al. 2016), in the North Pacific (Hosegood et al. 2006), and in the Southern Ocean (Viglione et al. 2018; du Plessis et al. 2019). By contrast, deep convection provides an extreme point in parameter space, typified by deep mixed layers (deeper than 500 m) and strong atmospheric forcing with typical monthly heat fluxes in winter of −400 W m^{-2} (Marshall and Schott 1999). Modeling studies helped to parameterize the effect of unresolved symmetric instabilities (Bachman et al. 2017) and to disclose their presence around convective region (Haine and Marshall 1998; Taylor and Ferrari 2010) while Straneo et al. (2002) focused on the parameter space of the Labrador Sea deep convection. Furthermore, symmetric instabilities were observed in convective regimes (Steffen and D'Asaro 2004; Bosse et al. 2021; Le Bras et al. 2022) in agreement with large lateral density gradients noticed during deep convection (Frajka-Williams et al. 2014).

To establish whether submesoscale flows actively restratify the Labrador Sea, three gliders sampled the deep convective region in winter 2020. First, deep convection is distinguished from restratification (section 3b) by discerning the edge of the convective region (gliders left the deep convective region before cessation of convection) from temporal restratification (gliders stayed in the deep convective region until restratification). Fresh and warm water intrusions by mesoscale eddies or filaments are found to participate in both spatial and temporal restratification (section 3d). Submesoscale instabilities

are then studied (section 4) to reveal that, alongside winter atmospheric forcing, submesoscale instabilities contribute to the decay of these intrusions and to restratify. Finally, a rough buoyancy budget suggests that winter baroclinic instabilities within the shallow freshwater layer of the Labrador Current balance half of the atmospheric buoyancy loss over the convective region (section 5). The remaining half seems to be balanced by warm eddies, which might originate from the West Greenland Current (Gelderloos et al. 2012).

2. Data and methods

a. Glider deployments

As part of the TERIFIC (Targeted Experiment to Reconcile Increased Freshwater with Increased Convection) project, two Kongsberg Seagliders (Eriksen et al. 2001), sg602 and sg638, were deployed offshore of Qaqortoq, southwest Greenland, from R/V *Adolf Jensen* in December 2019 and retrieved in Trinity Bay in Newfoundland, Canada, in May 2020. Unpumped CTDs (conductivity–temperature–depth) provided by Sea-Bird Electronics (CT sail) were mounted on both Seagliders with a sampling frequency of 0.1 Hz equivalent to every ~1 m in the vertical. The Seagliders sampled a total of 883 full-depth dive–climb cycles down to −1000 m in a sawtooth pattern. The average period and distance between apogees of full-depth dives is 6 h and 4.5 ± 0.8 km (mean ± standard deviation), which remains below the first baroclinic deformation radius of 8 km in the region (Gascard and Clarke 1983).

Another Teledyne Slocum glider (Pearldiver), with an extended energy bay, was deployed over eight months from St John's, Canada, as part of the HOTSeALS (Heat and Oxygen Transport Sensing Across the Labrador Sea) project. This Slocum glider was deployed offshore Newfoundland in December 2019 from a research cruise on board RRS *James Cook*, flying northward, arriving in the Labrador Sea in early January. Pearldiver flew at a slightly steeper pitch angle than the Seagliders with an average period and distance between apogees of full-depth dives of 4 h and 3.5 ± 0.6 km.

For Seagliders, inital processing with the University of Washington's base station (version 2.12) corrects for the thermal-inertia effect of the CT sail. This base station computes a hydrodynamic flight model (Bennett et al. 2021) with time-varying parameters (coefficients of lift and drag) to estimate the vehicle velocity, the depth-average current and the speed of water through the sensors used to correct for the thermal-inertia effect. Shallow salinity errors appeared sporadically for dives only in the top 50–100 m, likely due to a problem arising from a large Seaglider internal pressure. These anomalies as well as salinity spikes, potentially due to poor flushing of the conductivity sensor if the vehicle stalls or from biofouling, were discarded. The fields were optimally interpolated onto a 5-m and 1.5-km grid using a Gaussian weighting function with vertical and horizontal decorrelation length scales of 25 m and 8 km. Results presented below are not strongly affected by these choices of length scale and no artificial variability appears between raw and interpolated data. Cross calibration

between profiles from the two Seagliders and with delayed-mode Argo profiles within 15 km and 8 days for depths below 800 m indicates a fresh bias of 0.01 g kg^{-1} for sg638. Using similar temporal and spatial ranges, this offset was confirmed with Pearldiver, which was calibrated with high-quality CTD measurements during deployment.

b. Surface drifters

Along with the TERIFIC glider deployments, 50 drifting buoys (i.e., drifters) were launched in December 2019 offshore of Qaqortoq on the shelf break southwest of Greenland under the Global Drifter Program (GDP). The drifters were equipped with GPS, temperature sensors, and underwater drogues centered at 15-m depth that allow them to follow the surface currents of Fig. 1. The 6-hourly quality-controlled drifter data can be accessed via the ERDDAP website (Lumpkin and Centurioni 2019). Two buoys (WMO 6401816 and 6402537) are displayed in our analysis as they crossed the Labrador Current, or the 3000-m isobath, in February and in April 2020.

c. Ertel potential vorticity

The potential vorticity can be used to detect frontal flows that can sustain submesoscale instabilities following Thomas et al. (2013) but applied to glider data as in Thompson et al. (2016). Several instabilities can arise when the Ertel potential vorticity (PV) q and the Coriolis parameter f have opposite signs (Hoskins 1974) or alternatively when q is negative in the Northern Hemisphere:

$$q = (f\mathbf{k} + \nabla \times \mathbf{u}) \cdot \nabla b < 0 \tag{1}$$

with $b = -g\rho/\rho_0$ the buoyancy, g the gravitational acceleration, ρ the density, $\rho_0 = 1025$ kg m^{-3} a reference density, and with $\mathbf{u}$ the three-dimensional velocity. The total PV is separated to reveal the importance of the barotropic (q_{vert}) versus the baroclinic (q_{bc}) components in generating instabilities, $q = q_{\text{vert}} + q_{\text{bc}}$ with $q_{\text{vert}} = (f + \zeta)N^2$ and $q_{\text{bc}} = (\partial w/\partial y - \partial v/\partial z)(\partial b/\partial x) + (\partial u/\partial z - \partial w/\partial x)(\partial b/\partial y)$. The vertical relative vorticity, $\zeta = \partial v/\partial x - \partial u/\partial y \sim \partial v/\partial x$, is approximated by the depth-averaged current sampled by the glider in its cross-track orientation only v, following Thompson et al. (2016) with x being the along-track distance in the glider's direction. Several assumptions allow to estimate PV from glider measurements (Todd et al. 2016; du Plessis et al. 2019): neglecting the terms with vertical velocity w, neglecting the terms with nontraditional component of the Coriolis frequency (not shown), and assuming a thermal wind balanced flow with $|\partial \mathbf{u}_g/\partial z| = |\nabla_h b|/f$ or $v_z = b_x/f$ with z and x denoting partial derivatives. PV can be assessed from glider measurements to become $q_{\text{gl}} \sim (f + \zeta)N^2 - b_x^2/f$ with $N^2 = \partial b/\partial z$.

Using glider tracks to estimate the lateral buoyancy gradient b_x and to infer the wind-driven buoyancy flux can slightly underestimate these quantities because of limitations of gliders sampling across fronts, as discussed in Thompson et al. (2016). To partly compensate for this underestimation arising from the glider sampling, the depth-averaged current (DAC) is used to transform the cross-track coordinate system to a cross-stream coordinate system following Bosse and Fer (2019).

Using a Gaussian filter of width 8 km to remove abrupt anomalies of the DAC, the angle between the DAC and the axis perpendicular to the glider track is denoted ψ. The cross-front gradient and the along-stream velocities are the cross-track gradient and the across-track velocities increased by a factor $|1/\cos\psi|$. This factor is limited to 2 when the glider travels almost parallel to the flow (DAC) direction, i.e., within $\pm30°$ from it. In this case, the glider is parallel to a frontal current and can even be advected by strong eddy or boundary currents. In such instances, b_x might be underestimated although the glider might also travel in relatively quiescent regions. To account for these uncertainties surrounding the glider sampling of b_x, instances when the glider traveled within $\pm30°$ to the flow are highlighted below; they accounted for 34% of the glider measurements from mid-January to April.

The competition between vertical stratification, the shear of the geostrophic flow (through lateral stratification), and the vertical vorticity generates three instabilities (Thomas et al. 2013), identified by the finite balanced Richardson angle, $\phi_{\mathrm{Ri}_b} = \tan^{-1}(-|\partial\mathbf{u}_g/\partial z|^2/N^2)$. Gravitational instability (GI, or upright convection) occurs for $N^2 < 0$ and unimportant lateral stratification ($b_x \sim 0$), which is equivalent to $-180° < \phi_{\mathrm{Ri}_b} < -135°$. With stronger lateral stratification, symmetric instability (SI) can develop. A regime of mixed gravitational–symmetric instability occurs for $-135° < \phi_{\mathrm{Ri}_b} < -90°$ (with $N^2 < 0$) and SI are detected for $-90° < \phi_{\mathrm{Ri}_b} < \phi_c$ (with $N^2 > 0$). Using the vertical component of the absolute vorticity of the geostrophic flow $\zeta_g = f + \mathbf{k} \cdot \nabla \times \mathbf{u}_g$, the critical angle is $\phi_c = \tan^{-1}(-\zeta_g/f) \approx \tan^{-1}(-1 - v_x/f)$. In cyclonic conditions ($\zeta_g/f > 1$), $\phi_c < -45°$ whereas $\phi_c > -45°$ for anticyclonic vorticity ($\zeta_g/f < 1$) and centrifugal instability can develop for $-45° < \phi_{\mathrm{Ri}_b} < \phi_c$ (with $N^2 > 0$). Outside these unstable regimes, the flow remains stable for $\phi_c < \phi_{\mathrm{Ri}_b} < 0°$.

d. Wind-driven instabilities and mixed layer eddies

In the presence of a front, alongfront winds generate an Ekman transport of buoyancy across its lateral gradient (Thomas 2005) quantified by the Ekman buoyancy flux [EBF = $b_x\tau_y(\rho_0 f)^{-1}$] using the coordinates relative to the glider track or Q_{EBF} in equivalent heat flux [$Q_{\mathrm{EBF}} = -\mathrm{EBF} \times \rho_0 c_p/(g\alpha)$] with c_p the specific heat of seawater and α the thermal expansion coefficient. Destabilizing downfront winds (wind stress oriented in the direction of the geostrophic shear) advect denser waters above lighter waters resulting in increased convection ($Q_{\mathrm{EBF}} < 0$ or EBF > 0) while upfront winds restratify the boundary layer ($Q_{\mathrm{EBF}} > 0$ or EBF < 0). τ_y is the alongfront wind stress component, which is projected in the geostrophic flow direction that is inferred from the DAC (du Plessis et al. 2019); τ is estimated from the 10-m wind components of the ERA5 reanalysis (Hersbach et al. 2020) with hourly temporal and 1/4° spatial resolutions.

In frontal regions, submesoscale ageostrophic baroclinic instabilities subsequently appear over longer time scales and lower lateral stratification than SI, and persist for nonnegative PV as well. Mixed layer eddies (MLE) restratify the mixed layer by slumping isopycnals and transferring lateral buoyancy gradient into vertical stratification, thus injecting denser

water below lighter water. This restratification depends on b_x and H through an eddy-driven overturning streamfunction (Fox-Kemper et al. 2008) that parameterizes the upward buoyancy flux ($w'b' > 0$), responsible for transferring available potential energy into kinetic energy, and becomes in equivalent heat flux $Q_{\mathrm{MLE}} = 0.06b_x^2 H^2 c_p \rho_0 (\alpha g f)^{-1}$ (Mahadevan et al. 2012). The spatial gradient b_x is estimated from the optimally interpolated density and the MLD, H, is defined by a density threshold of $\delta\rho = 0.01$ kg m^{-3} relative to a shallow reference at 10 m (Thomas et al. 2015).

e. Convective layer depth

The convective layer depth, h, separates a regime where upright convection prevails ($-h \leq z$) from a regime of slantwise convection where SI can exist at $-H \leq z \leq -h$ (Taylor and Ferrari 2010). The lower limit of the low-PV boundary layer is approximated by the MLD as in Yu et al. (2019), given the expected agreement between these two layers (Taylor and Ferrari 2010). The convective layer depth is retrieved from the buoyancy and momentum equations depth-integrated over this layer (Taylor and Ferrari 2010)

$$\left(\frac{h}{H}\right)^4 - c^3\left(1 - \frac{h}{H}\right)^3 \left(\frac{w_*^3}{|\Delta u_g|^3} + \frac{u_*^2}{|\Delta u_g|^2}\cos\theta\right)^2 = 0. \quad (2)$$

The natural Rossby number $\mathrm{Ro}^* = (B_0/H^2 f^3)^{1/2}$ quantifies whether rotation can affect convection with $\mathrm{Ro}^* < 1$ (Maxworthy and Narimousa 1994; Jones and Marshall 1993). Given an average Ro^* of 0.5 over January–March, the effect of rotation on convective plumes is retained in the scaling of vertical velocity fluctuations, which becomes $w_* = (B_0/f)^{1/2}$. The surface buoyancy flux is $B_0 = -g\alpha Q_{\mathrm{HF}}/(\rho_0 c_p) + g\beta(E - P)S_0$, with β the haline contraction coefficient and S_0 the surface salinity. The term Q_{HF} is the surface heat flux, and $E - P$ is the rate of evaporation minus precipitation, which are both extracted from the ERA5 reanalysis. The term θ is the angle of the wind vector relative to the geostrophic shear vector, c is a constant ($c = 14$), $u_* = \sqrt{(\tau/\rho_0)}$ is the frictional velocity, and $|\Delta u_g|$ corresponds to the geostrophic velocity change over the ML. By definition, h remains within H, and SI becomes important when $h/H < 1$, whereas convection prevails within the ML for $h \approx H$.

Submesoscale instabilities extract their kinetic energy from convective available potential energy (for gravitational instability) or from the vertical shear of geostrophic fronts (for symmetric instability) before being dissipated at smaller scales (Gula et al. 2021). In upright convection, the turbulent kinetic energy production results from the positive vertical turbulent buoyancy flux within the convective layer ($-h \leq z$) as a result of destabilizing surface buoyancy loss. Below the convective layer but within the boundary layer ($-H \leq z \leq -h$), mean kinetic energy extracted from the balanced front by SI is predominantly converted into turbulent kinetic energy at a rate given by the geostrophic shear production (Taylor and Ferrari 2010); a conversion that is followed by a geostrophic adjustment and flattening of isopycnals. Additionally, SI and their slanted overturning circulations are associated with secondary shear instabilities, which can inject and mix high-PV surrounding
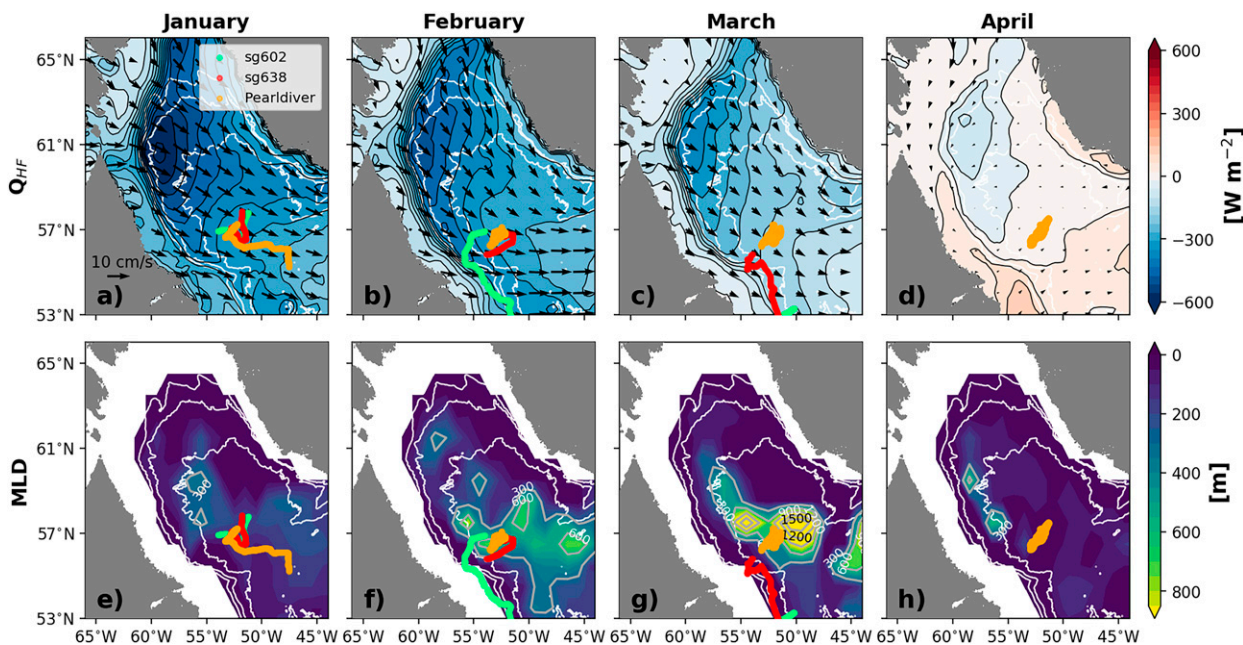
FIG. 2. (top) Surface heat flux and winds (arrows) obtained from the ERA5 reanalysis and (bottom) mixed layer depth estimated from a monthly Argo climatology (Roemmich and Gilson 2009) for (a),(e) January, (b),(f) February, (c),(g) March, and (d),(h) April 2020 with the monthly trajectories of each glider (colored dots).

waters with the unstable flow (Taylor and Ferrari 2009; Thomas et al. 2013). These shear instabilities tend to stabilize and restratify the unstable layer by increasing the PV close to a neutrally stable state ($q \sim 0$). Therefore, SI can oppose the destabilizing wind-driven and surface buoyancy fluxes when $B_0 + \text{EBF} > 0$, which can lower PV below 0.

3. Labrador Sea deep convection

First, we present the large-scale atmospheric conditions for the Labrador Sea in winter 2020. The atmosphere modulates the deep convection together with the oceanic preconditioning. Given these background conditions, the glider deployments are then described relative to the deep convective region, along with the spatial and temporal boundaries of this region.

a. Atmospheric forcing

Recently, the extreme winter of 2015, with record oceanic heat loss, was associated with very deep convection, i.e., MLD below 1700 m, (Yashayaev and Loder 2016), and was followed by several years of MLD deepening down to 2000 m, partly resulting from oceanic preconditioning (Yashayaev et al. 2020). In contrast, moderate atmospheric conditions led to shallower MLD around 1400–1500 m in winter 2019. Furthermore and despite the high-NAO (North Atlantic Oscillation) condition of winter 2020, with the NAO index defined as the sea level pressure difference between the subtropical Azores high and the subpolar Icelandic low, this winter was characterized by mild conditions relative to winter climatologies of the past four decades (Yashayaev et al. 2020). These conditions

were moderate westerly winds along the Labrador coast, warm sea surface temperature, and low sea ice extent.

The monthly maximal heat loss to the atmosphere (~ -600 W m^{-2}) typically occurs in January in the northwest corner of the Labrador Sea (Fig. 2a) where cold and dry westerlies from eastern Canada blow offshore and intensify the heat flux by increasing the air–sea temperature gradient. This large-scale atmospheric pattern is reminiscent of a positive phase of the NAO index as confirmed by an index of 1.83 in winter 2020 (Hurrell 2022). Enhanced westerly winds and frequent storms are linked to a positive NAO, which contributes to modulate the interannual variability of deep convection (Dickson et al. 1996), and to bring large heat loss further south and eastward (Pickart et al. 2002) in the central Labrador Sea in Fig. 2a. As a result in March 2020, the deepest MLD (down to 1500 m in Fig. 2g) from a monthly Argo climatology (Roemmich and Gilson 2009) along with the densest surface density of the Labrador Sea appear in the southwest Labrador Sea before restratifying, as indicated by the shoaling MLD in April (Fig. 2h).

b. Glider deployments around the convective region

In the winter of 2020, the three gliders arrived at the deep convection region (Fig. 2e) in January before the onset of convection when MLD $\sim$100–200 m. Of the three gliders, Pearldiver performed transects of about 200 km long from around (56.2°N, 53.5°W) to (57.5°N, 51.2°W) throughout the winter. It remained in the region until May 2020 before transiting south to Trinity Bay, Newfoundland, for recovery. The two Seagliders (sg602 and sg638) stayed in the central Labrador Sea until February 2020, and then transited southwestward toward the more stratified Labrador Current (Fig. 2f).
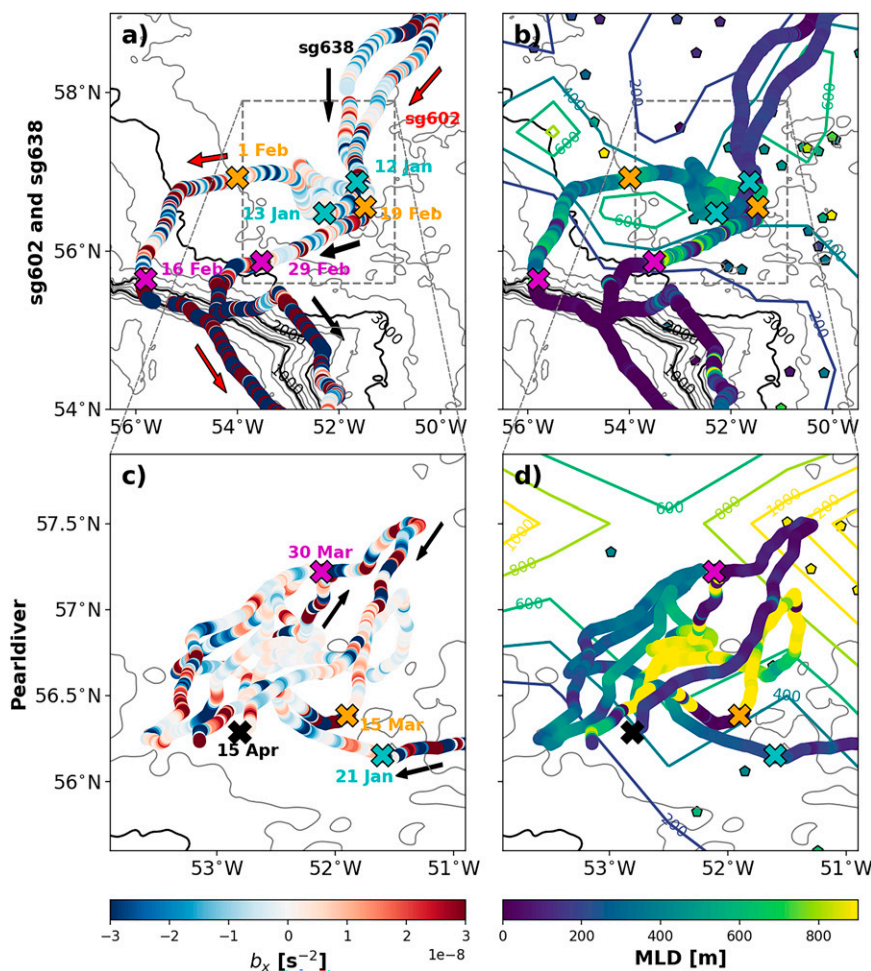
FIG. 3. Lateral buoyancy gradient within the mixed layer depth along the glider tracks of (a) sg602 (along the red arrows) and sg638 (along the black arrows) and of (c) Pearldiver. Mixed layer depth along the glider tracks (colored points), and from Argo profiles (colored pentagons and contours) in (b) February and (d) March 2020. The cyan, orange, and magenta dates/crosses correspond to the start of the convective period, the start of the restratifying period, and the restratification's end date, respectively, which are defined in Fig. 4. The displayed trajectory of Pearldiver ends on 15 Apr (black cross) in (c) and (d).

As the two Seagliders left the region, they encountered variable MLDs (ranging from 30 to 860 m) during a ~2-week period (Figs. 4b,c) and spanning ~200 km (Fig. 3b). During this period, the net heat fluxes were still cooling (removing buoyancy from) the ocean (Fig. 4a). During Pearldiver's mission, the ocean was restratified from around 30 March (Figs. 3d and 4d). Furthermore, the Argo floats also indicate that the deepest MLDs below 1000 m are found in March in the northeast corner of Fig. 3d, in a region where the glider track observed shallow MLD above 50 m in the first days of April. Therefore, restratification is believed to have occurred for most of the deep convection region around 30 March, which is referred to below as the restratification's end date. Like the Seagliders, Pearldiver also observed more variable MLDs (ranging from less than 50 to 1000 m) during the end of convection (15–30 March) and the net heat fluxes became positive in late March (Fig. 4a).

Because the Seagliders were transiting from the convective region to a region which never experiences deep convection (the Labrador shelf), we call the restratification observed by the Seagliders "the edge of the convective region," where stratification appears in the dataset as the Seagliders move through space. Since Pearldiver remained in the region of convection for the whole winter (until May), we call the restratification observed by Pearldiver a "temporal restratification," or increase in stratification which appeared with time. The changes sampled by a glider can be decomposed into

$$\frac{D}{Dt}_{\text{glider}} = \frac{\partial}{\partial t} + u_{\text{water}} \frac{\partial}{\partial x} + u_{\text{glider}} \frac{\partial}{\partial x}. \quad (3)$$

The temporal restratification corresponds to $\partial/\partial t$, while the edge of the convective region, i.e., where the glider translational velocity is moving through a horizontal gradient from
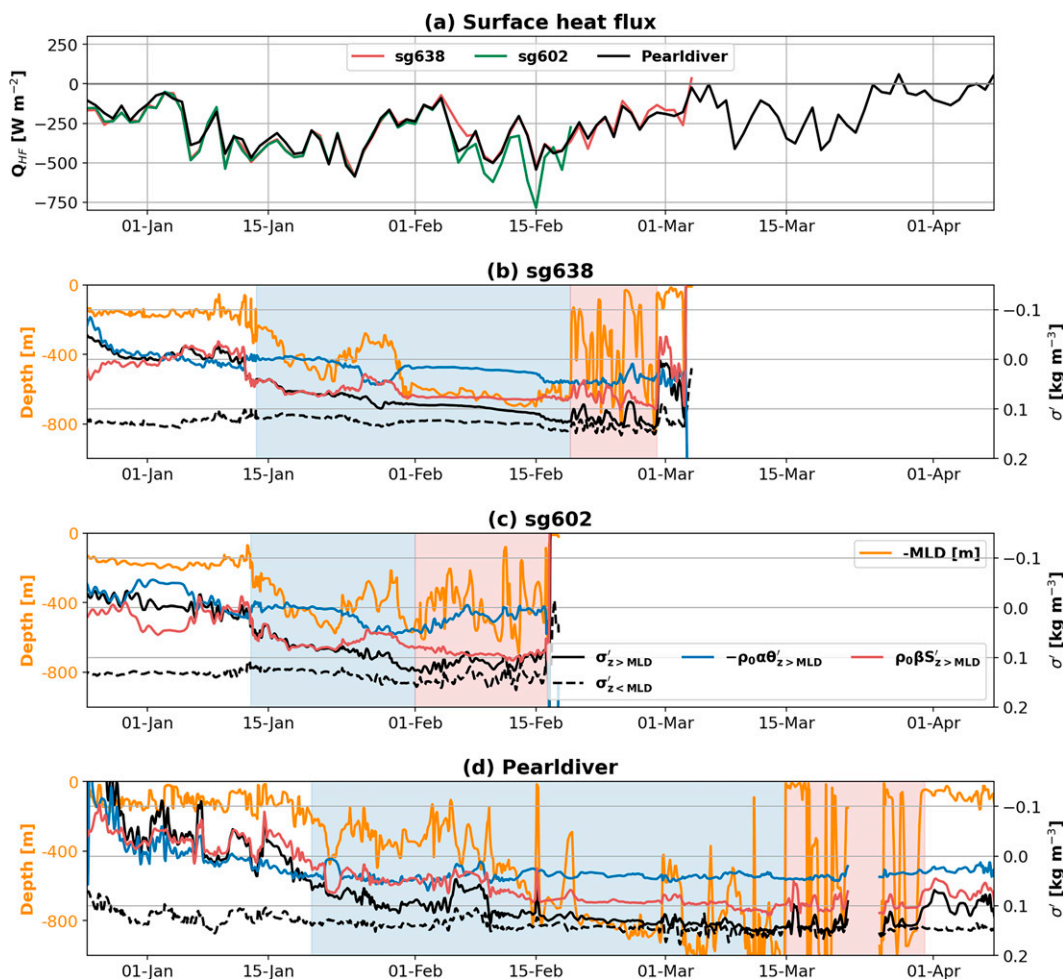
FIG. 4. (a) Surface heat flux Q_{HF} above each glider track. Temperature (blue) and salinity (red) contributions to density anomalies (black; scaled by $\rho_0\alpha$ and $\rho_0\beta$) depth averaged within the mixed layer (full lines) and below it (for density in dashed lines for MLD $> z > -1000$ m) for each glider: (b) sg638, (c) sg602, and (d) Pearldiver. MLD is displayed in orange (along the left y axis). Convective periods (blue shading) start when MLD deepens below 200 m. Restratifying periods (red shading) are characterized by highly variable MLD (i.e., daily MLD standard deviation > 80 m) that precedes the restratification's end date, which occurs when the MLD shallows to 50 m (at the end of red shading).

unstratified toward stratified waters corresponds to $u_{\mathrm{glider}}\partial/\partial x$. In our formulation, we are not distinguishing the advective term ($u_{\mathrm{water}}\partial/\partial x$), which still projects on the glider measurements D/Dt_{glider}. The advective term and $u_{\mathrm{glider}}\partial/\partial x$ should have the same order of magnitude given the mean $|u_{\mathrm{water}}|$ of 0.12 m s^{-1} approximated by the DAC and the mean $|u_{\mathrm{glider}}|$ of 0.22 m s^{-1}.

c. Deep convection

In the convective region, the maximal MLD remains between 600 and 800 m in February (Figs. 3b and 4b,c) and then deepens below 1000 m in March (Figs. 3d and 4d). As this MLD is below the maximum dive depth of the gliders, we cannot observe the MLD at this time, but these depths are consistent with the MLDs observed by Argo profiling floats (Figs. 2g and 3d). The timing of the maximum MLD is roughly two months after the maximum surface heat loss (Fig. 2a).

Deep MLDs are not restricted to the central Labrador Sea, but are also present inshore of the 3000-m isobath on the continental slope off Labrador (e.g., sg602 in Fig. 3b) as previously observed (Pickart et al. 2002; Cuny et al. 2005).

During deep convection, Labrador Sea Water (LSW) formation occurs through densification of near surface waters (in the surface mixed layer). The ML density, $\sigma'_{z>\mathrm{MLD}}$, increases toward the deeper and denser waters, $\sigma'_{z<\mathrm{MLD}}$, over the period from January to mid-February (black and black dashed in Figs. 4b–d), with the prime denoting an anomaly relative to $\Theta = 3.5°C$ and $S_{\mathrm{A}} = 34.85$ g kg^{-1}. Decreasing temperatures dominate the change in mixed layer density in early January (blue in Figs. 4b–d, especially in Figs. 4b and 4d). Deep convection begins in the middle of January, here defined as MLD deeper than 200 m (orange lines in Figs. 4b–d) with the convective periods indicated by blue shading. From mid-January, the mixed layer densification is mostly dominated by increases in salinity (rather than decreases in temperature) as shown in
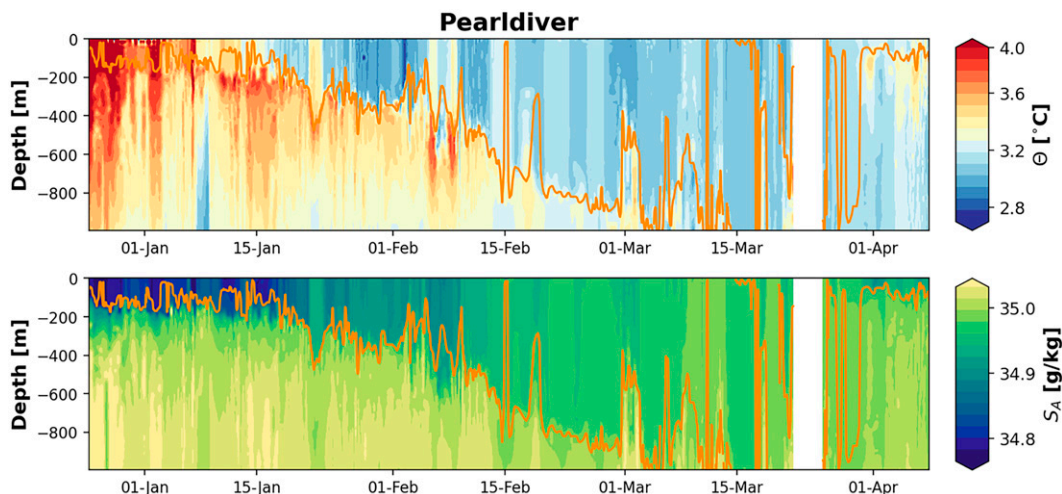
FIG. 5. Conservative temperature and absolute salinity sampled by Pearldiver with MLD (orange). The data gap in late March results from issues with the onboard computer of Pearldiver.

Figs. 4b–d (where the red lines, showing the salinity contribution to density, track the overall changes in mixed layer density $\sigma'_{z>\mathrm{MLD}}$ given by the black lines). The source for this saltier water is the salty deep waters below the mixed layer which are entrained into the mixed layer as the mixed layer deepens.

This pattern is particularly apparent in the records from Pearldiver (Fig. 5). The waters observed by Pearldiver decrease in temperature from 28 December to 20 January, with no subsequent decreases. However, the increase in density of the mixed layer waters continues from 20 January through 15 February, due to increases in salinity concurrent with the mixed layer deepening from around 400 to 800 m deep. As MLD deepens, winter convective mixing injects cool and fresh upper-layer waters at depth, while warm and salty lower-layer waters (from below the ML in Fig. 5) enter the upper layer as estimated by Straneo (2006a). The resulting ML heat gain is likely balanced by atmospheric heat loss and potential lateral heat flux as indicated by the constant ML temperature in February–March at the deep convection site (Fig. 4d).

The pattern of changes over the winter to spring season can also be seen in individual profiles (Figs. 6a–c) and in Θ–S space (Figs. 6d,e). In Θ–S space, we see the temperature decrease and salinity increase in January (arrow 1 in Fig. 6e). From February to March, the temperature remains roughly constant but salinity increases (arrow 2). Finally, the temperature increases and salinity decreases from March to April (arrow 5). These mixed-layer-averaged properties illustrate the observed seasonal cycle.

Vertical profiles of temperature, salinity and density allow us to quantify the contribution of property anomalies to the integrated buoyancy content anomaly ΔB (Schmidt and Send 2007). Here, ΔB is taken relative to the maximal convection—or densest profile in mid-March (lightest purple, σ_{ref})—and integrated over the top $h_2 = 400$ m to capture the averaged vertical extent of the lateral intrusions presented below, $\Delta B = -(g/\rho_0)\int_{h_2}^0 (\sigma - \sigma_{\mathrm{ref}})dz$. Using the equation of state, the temperature $\{\Delta B_\Theta = g\int_{h_2}^0 [\alpha(T - T_{\mathrm{ref}})]dz\}$ and salinity

$\{\Delta B_S = -g\int_{h_2}^0 [\beta(S - S_{\mathrm{ref}})]dz\}$ components are further isolated with $\Delta B = \Delta B_\Theta + \Delta B_S$.

Pearldiver (Fig. 5) sampled a convection–restratification cycle shown by two equivalent density profiles (Fig. 6c) from mid-January (dark purple) with $\Delta B = 36 \times 10^{-3}$ m^2 s^{-2} to late April (dark brown) with $\Delta B = 28 \times 10^{-3}$ m^2 s^{-2}. The initial temperature loss reduces the buoyancy by $\Delta B_\Theta = -12 \times 10^{-3}$ m^2 s^{-2} while the subsequent salinity gain by vertical entrainment brings $\Delta B_S = -23 \times 10^{-3}$ m^2 s^{-2} (labels in Fig. 6b) from mid-January to mid-March. This cycle, shown as a time series in Fig. 4d and with vertical profiles and mixed layer properties (Fig. 6), underlines the key role of entrained deep salty waters in increasing the ML density and also hints at the important and unexpected role of freshwater during restratification.

d. Restratification by either fresh or warm water

In the convective region (Fig. 5, Pearldiver), stratification (MLD < 100 m) keeps deep cool and fresh LSW away from atmospheric forcing in late March. After restratification in April, deep waters below the mixed layer increase in temperature and salinity (Fig. 5) potentially influenced by lateral fluxes of adjacent Irminger Water (Straneo 2006a). Despite sudden restratification, with MLD shoaling by ~600 m over less than a day in late March (or alternatively, a glider sampling varying MLD over ~18 km), several intrusions of relatively freshwater decrease the density $\sigma'_{z>\mathrm{MLD}}$ (black in Fig. 4d) by as much as −0.06 kg m^{-3} from mid-March [as also seen with arrow (3) from light purple to light orange pentagons in Fig. 6e]. During this restratifying period (red shading in Fig. 4d), negative changes in density are dominated by salinity changes rather than temperature. Anomalies in glider-observed densities are correlated with their salinity contributions (correlation coefficient $r = 0.9$, $p < 0.01$, and with a slope a of the linear least squares fit of 0.85), whereas temperature contributions are less well correlated with density anomalies ($r = 0.35$, $p < 0.01$, and a slope of $a = 0.15$). The salinity and temperature contributions
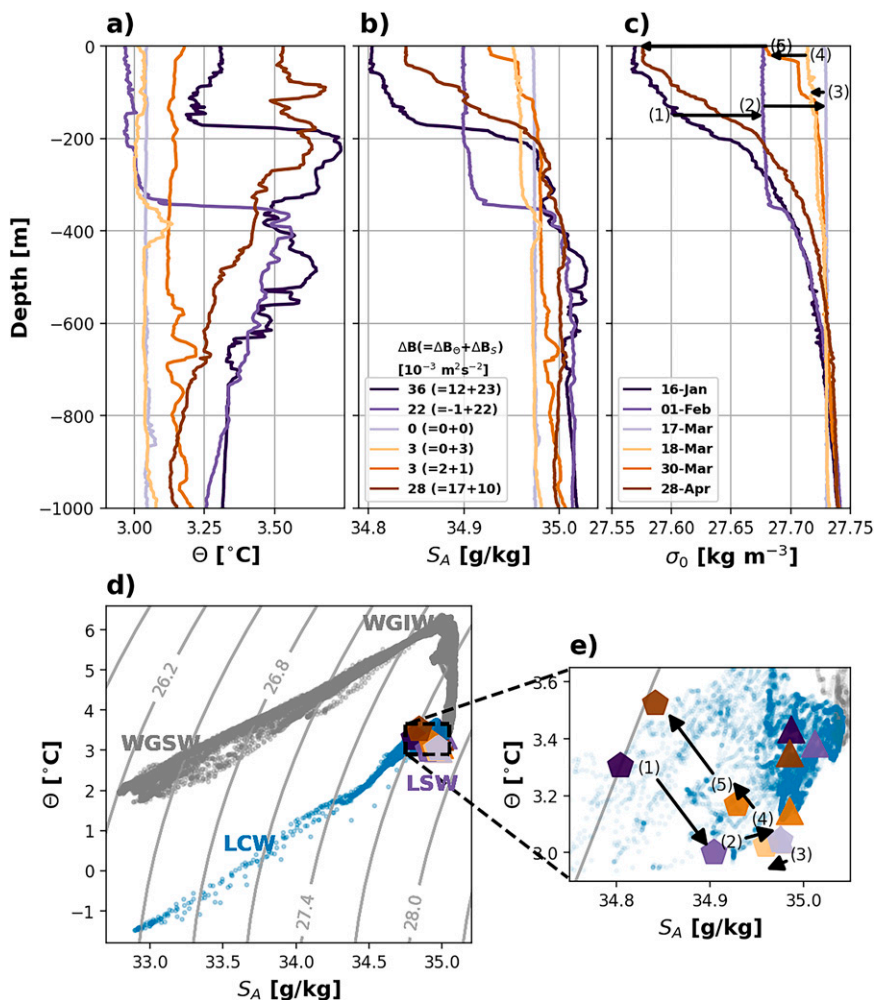
FIG. 6. Convection–restratification cycle at the deep convection region (Pearldiver) from January (dark purple) to April (dark brown) in (a) temperature, (b) salinity, (c) density, and (d),(e) in Θ–S_A space depth-averaged within (pentagon) or below (triangle) the ML. Buoyancy anomaly (ΔB) with its Θ and S_A components relative to the deepest convection (lightest purple) integrated over the top 400 m [legend in (b)]. The Θ–S_A properties of waters sampled inshore of the 2000-m isobaths by sg638 are added in (d) and (e): West Greenland Shelf Water (WGSW), West Greenland Irminger Water (WGIW), Labrador Current Water (LCW), and Labrador Sea Water (LSW).

are not independent of the density anomalies but the stronger correlation with salinity (and additionally, the stronger slope of the correlation) indicates a salinity dominance to the density changes. Along with the subsequent shallow ML freshening from 30 March (Figs. 4d and 5b), these freshwater events or intrusions highlight the prevalent role of lateral freshwater fluxes in terminating convection.

Furthermore, the changes in stratification observed by sg638 from 20 to 28 February (Fig. 4b) occurred as the glider transited spatially from a more central, deeply convecting region toward a more stratified boundary offshore from the Labrador shelf. This "spatial" restratification suggests that fresh anomalies at the boundary of the actively convecting region are playing a role in shoaling the mixed layer depth, where changes in mixed layer salinity dominate changes in

mixed layer density (correlation coefficient of $r = 0.84$ between the salinity contributions to density and density anomalies, $p < 0.01$, and $a = 0.95$). The salinity anomalies observed by sg638 changed over short temporal (less than 1 day) and spatial scales. While we cannot conclusively say whether these salinity anomalies are due to temporal or spatial changes, they do indicate a high degree of salinity variability within short temporal and spatial spans.

Small salinity variability at the convection site in late February (compared with late March, Fig. 4d) suggests that freshwater intrusions might first occur at the convection boundaries before affecting the core of the convective site. This observation is supported by strong lateral buoyancy gradients that appear first at the edge of the convection region in February (Fig. 3a) before appearing in its center in late March (Fig. 3c). This may

explain the late occurrence of a freshwater pulse in the convective region in April–June identified by Schmidt and Send (2007) despite lateral freshwater fluxes being present previously in winter at the convection boundaries. Focusing on the convective region may overemphasize the maximum sea surface salinity in March (Gelderloos et al. 2012) expected from the deep upward salinity flux mentioned above.

At the edge of the convective region sampled by sg602, on the other hand, the density anomalies are more strongly correlated with their temperature contributions (correlation coefficient $r = 0.86$, $p < 0.01$, and $a = 1.13$, Fig. 4c). It is possible that steeper topography below the transect of sg638 than sg602 (Fig. 3) could trigger instabilities from the inshore shallow freshwater Labrador Current, favoring the generation of small, fresh eddies; however further work would be needed to investigate this hypothesis. These warm intrusions sampled between the deep convection site and the Labrador Current (Fig. 4c) should contribute to warm the deep convection site (arrow 4 in Fig. 6e) along with intrusions of diluted West Greenland Shelf/Irminger Water (Hátún et al. 2007).

The Θ–S plot of Pearldiver (Fig. 6e) along with sg602 indicate that both fresh and warm water intrusions bring buoyancy to the deep convection site before the restratification's end date on 30 March (Fig. 4d), while the surface heat flux is still transitioning from negative to positive (Fig. 4a). At the restratification's end date, 10% of the buoyancy that was lost to the atmosphere is replenished (Fig. 6b) but the accumulated positive heat flux at the surface only accounts for 0.2% of the negative heat flux at the surface. Therefore, the atmospheric heat flux might not play a predominant role in the restratification compared with the lateral flux of fresh and warm water. Warm intrusions bring twice as much buoyancy than fresh intrusions before restratification on 30 March (label in Fig. 6b). This ratio remains unchanged in April once the atmosphere starts to warm the ocean.

e. Origin of freshwater intrusions

Although strong uncertainties exist in estimates of evaporation minus precipitation ($E - P$) in the Labrador Sea, precipitation is believed to dominate over evaporation over the full seasonal cycle, with a maximum in freshwater gain in winter (Sathiyamoorthy and Moore 2002). This flux, however, is unable to fully explain the shallow (top 200 m) spring freshening of the deep convection region observed by Lazier (1980) and Straneo (2006a), which accounted for an addition of $\sim$20 cm of freshwater to the water column in spring (Schmidt and Send 2007). In our case, in March 2020 from densest convection to restratification (from 17 to 30 March in Fig. 6b), the gliders observed a reduction in salinity in the top 100 m by 0.02 g kg^{-1} with daily events capable of reducing salinity by 0.01 g kg^{-1}, for example in the top 400 m on 18 March. The $E - P$ also adds buoyancy over the glider tracks during winter 2020. However, winter $E - P$ only balances $\sim$2% of the total buoyancy loss by the surface heat flux, in agreement with a previous estimate of 3% for the 1990s (Lazier et al. 2002). The daily freshwater events are thus more likely to originate from lateral intrusions, such as eddies or filaments.

The West Greenland Current is often expected to be the source of fresh and warm water found in the central Labrador Sea (Hátún et al. 2007; Rykova et al. 2009; Gelderloos et al. 2011). Hátún et al. (2007) have been able to link eddies found several hundred kilometers north of the convective patch with the WGC. However, in trying to determine the source of the freshwater observed by the gliders (several tens of kilometers south of the convective patch), we believe that the Labrador Current cannot be excluded as a potential source of freshwater to the convection region. This is due both to the proximity of this strong source of freshwater, but also based on Θ–S_A relationships, a couple of drifter trajectories, local wind conditions and some supporting evidence from satellite data.

From the Θ–S_A diagram, the fresh event from 18 March is indicated by arrow 3 in Fig. 6e. This arrow points to the left toward fresher water without a change in temperature. The Labrador Current waters (also plotted on the diagram) are also fresher and not warmer, whereas the West Greenland Current observations were both fresher and warmer. By a simple mixing argument, the change in properties would have an angle relative to constant temperature if the source waters were from the WGC.

In February and in early April, two surface drifters crossed from the Labrador Current to the offshore region (green and magenta, respectively, Fig. 7). By themselves, these trajectories show that it is possible that some freshwater may escape from the Labrador Current into the surrounding deep waters. For the most part, the wind direction here is in the westerly/ northwesterly direction (Fig. 2) which would result in onshore Ekman transport. During some periods (about 22% of the time over the drifter tracks of Fig. 7), winds are in the easterly direction, including just prior to the offshore movement of the magenta trajectory (around 56.5°N and 57°W). Overall, the winds suggest that the background wind conditions are in the onshore direction, though intermittent storms and wind gusts could still be responsible for offshore transport of freshwater.

We further explore (Fig. 7) the hypothesis that the observed freshwater eddies originate from the Labrador Current by investigating data from the multiscale ultra-high-resolution (MUR) sea surface temperature (SST) product (Chin et al. 2017) along with sea level anomalies (SLA) obtained from the 1/4° resolution AVISO altimetric product. SLAs are obtained from the difference between sea surface height and the mean sea surface averaged from 1993 to 2012. The SST product combines in situ data from three satellites: the highest resolutions (around 1 km and around 4–8.8 km) come from a high-resolution infrared sensor and from an AVHRR (Advanced Very High Resolution Radiometer) infrared sensor, respectively, which are both particularly affected by the cloud coverage, as opposed to the microwave sensor with a sampling resolution of 25 km.

Freshwater anomalies should coincide with cool anomalies, which do appear between the convective region and the Labrador Current (Fig. 7). Even so, as seen from the glider trajectory (Fig. 7), sg638 crossed a day later (on 23 February) a cool and fresh eddy with a radius of $\sim$50 km and an SST anomaly of $\sim$0.1°C. These anomalies seem to correspond to a density anomaly found over the top 400 m (Fig. 8b, and in Θ and S not shown). Just southwestward, another fresh but warm eddy
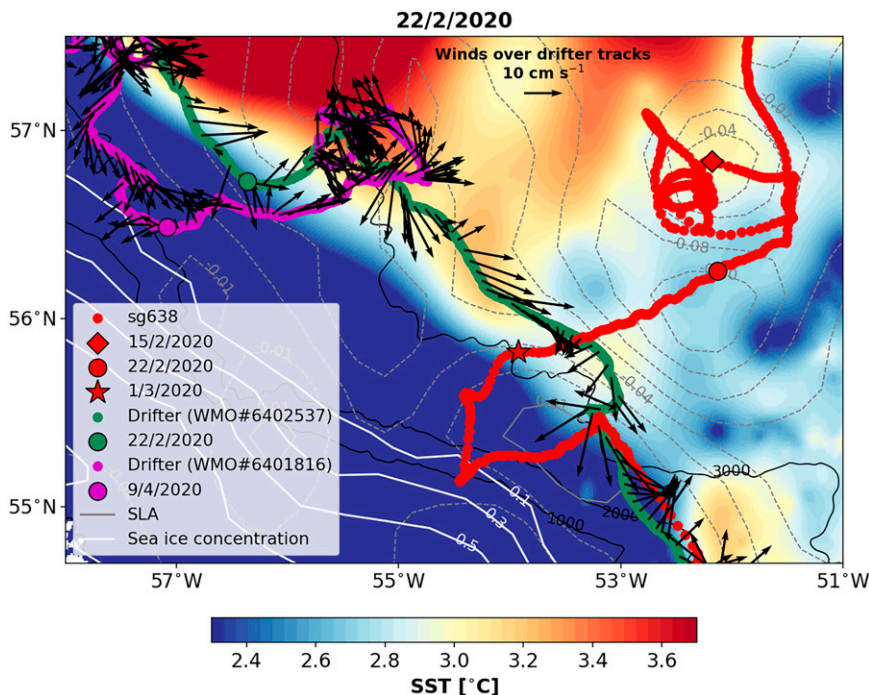
FIG. 7. Sea surface temperature for the 22 Feb 2020 around the Labrador Current (dark blue temperature) and Hamilton Banks (southeast corner) with the trajectory of sg638 (red) and its daily location (red circle) traveling from the deep convection region (red pentagon, 15 Feb) to the Labrador Current (red star, 1 Mar). Two surface drifters traveled offshore from the Labrador Current in February (green) and in April (magenta). The wind vectors over the drifter trajectories are added (arrows). SLA (m) are displayed in gray. Contours of daily sea ice concentration (white) and isobaths (black) are added.

(Fig. 7) was sampled by sg638 on 26 February, with property anomalies found in the top 200 m (Fig. 8b). They appeared to have originated in the Labrador Current along with another cold eddy to the west (Fig. 7). The winter cloud cover, however, limits the SST spatial resolution, which is generally coarser than 1 km in Fig. 7; it also precludes the establishment of a direct link between the shallowest temperature of sg638, where the glider-observed near-surface temperatures are outside a standard deviation (Chin et al. 2017) from the MUR SST. Altimetric data show a local maximum in eddy kinetic energy (near the Labrador Current, Fig. 1), suggesting meanders of the current or the generation of eddies, but generally the data are too coarse to resolve the local mesoscale, as seen from the SLA in Fig. 7. The upcoming SWOT (Surface Water and Ocean Topography) mission (Morrow et al. 2019) might help in the future to establish the eddy origin. Altogether, these strands of evidence suggest a potential role for freshwater from the Labrador Current to reach the region of deep convection, but are not fully conclusive. Future work would be needed to clarify the role of Labrador Current instabilities in freshwater exchange on the west side of the Labrador Sea.

4. Submesoscale instabilities

The potential role of frontal currents, arising at filaments and eddy boundaries, in restratifying the convective region of the Labrador Sea is now investigated. Overall, we find relatively large lateral gradients in buoyancy within the surface mixed layer. These can be seen visually in a map (Fig. 3a), but can also be quantified by the lateral buoyancy gradient along the glider track b_x. Here we consider a lateral gradient greater than a threshold of $10^{-8} \, \text{s}^{-2}$, and find that this occurs 49% of the time during the restratifying periods (red shading in Fig. 4) and only 25% of the time during actively convecting periods (blue shading in Fig. 4). In the Labrador Sea, where wintertime vertical stratification is low over the top 500–1000 m, it is somewhat surprising that horizontal density gradients of this magnitude (up to $3 \times 10^{-7} \, \text{s}^{-2}$) can persist. These substantial horizontal density gradients suggest a potential role for submesoscale instabilities in the restratification of the region prior to the period when the atmosphere actively warms the surface ocean.

To investigate submesoscale instabilities, we show in Fig. 8 the surface heat flux over the glider track, observed seawater density, lateral buoyancy gradients (b_x), observed PV (q_{gl}), and gradient Richardson number (ϕ_{Ri_b}). The gray shading underlines the potential underestimation of b_x when the glider direction was aligned with the geostrophic flow. Regions of negative PV (Fig. 8d) show areas where submesoscale instabilities may be occurring, while the gradient Richardson number ϕ_{Ri_b} can be used to classify which instabilities are permitted (Fig. 8e). For example, before 19 February, the lateral buoyancy gradients b_x were small and the periods with
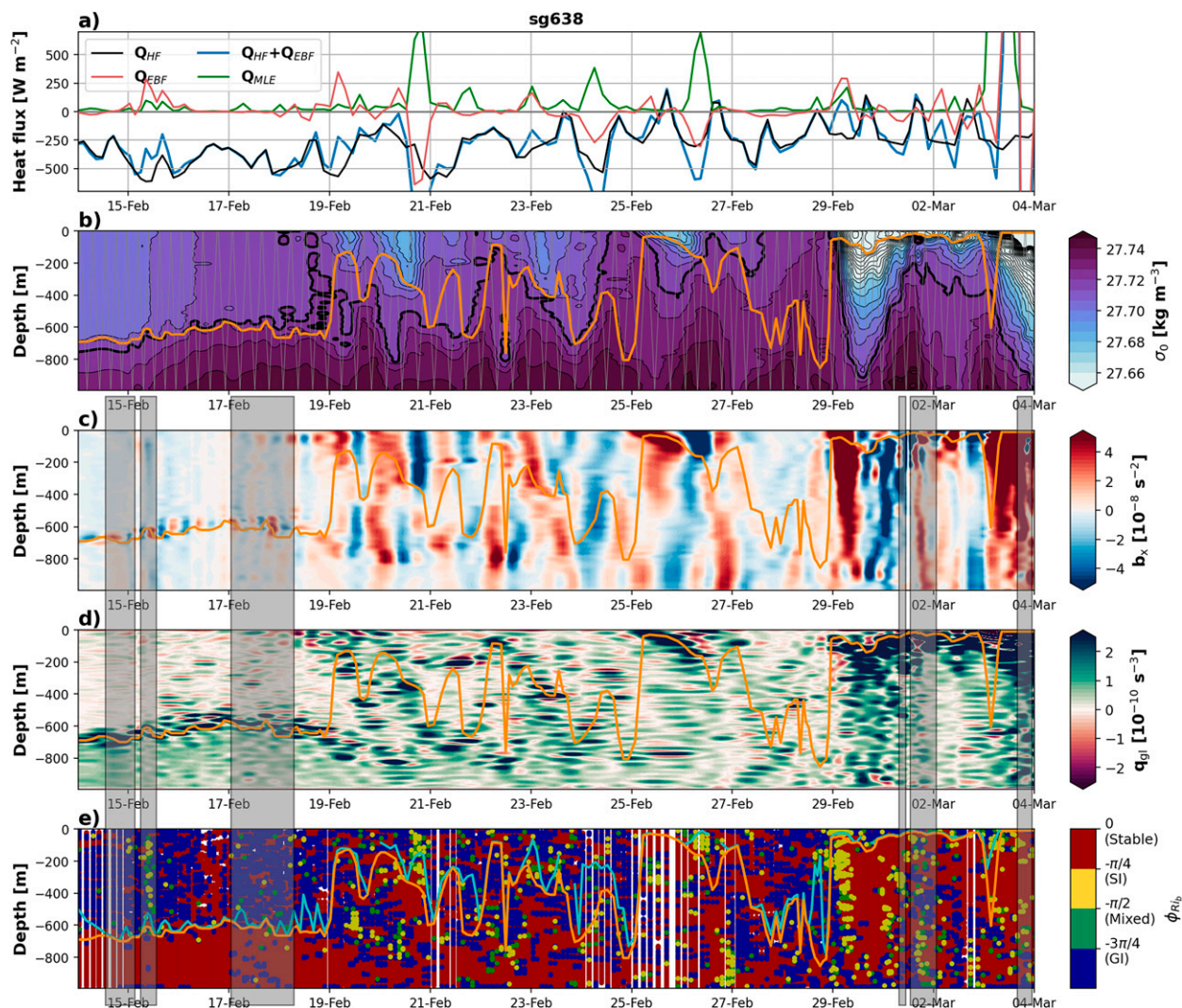
FIG. 8. (a) Surface heat flux Q_{HF} (black), Ekman (Q_{EBF}, red), and mixed layer eddy (Q_{MLE}, green) buoyancy fluxes in equivalent heat flux; $Q_{\mathrm{HF}} + Q_{\mathrm{EBF}}$ is in blue. Negative heat flux destabilizes surface waters. (b) Potential density measured by sg638 with the glider tracks (gray). The thick black line ($\sigma_0 = 27.72$ kg m^{-3}) indicates the upper limit of Labrador Sea Water. (c) Lateral buoyancy gradient b_x. (d) Potential vorticity estimated from glider measurements q_{gl}. (e) Overturning instabilities arising for negative potential vorticity: gravitational instabilities (GI in blue), symmetric instabilities (SI in yellow), mixed regime gravitational/symmetric instabilities (Mixed in green); and stable conditions (red). The mixed layer depth $-H$ is indicated in orange in (b)–(e) and the convective layer depth $-h$ is added in cyan in (e). The gray shading highlights instances when the glider traveled within $\pm 30°$ to the flow (DAC) direction, which might denote an underestimation of b_x in (c).

negative PV ($q_{\mathrm{gl}} < 0$) were primarily due to gravitational instabilities (blue dots in Fig. 8e). After 19 February, sg638 was crossing the actively convecting region toward the stratified Labrador Current (arrived around 4 March, visible with the low density in Fig. 8b). The other occurrence of lower-density water on 29 February was likely an eddy, which escaped from the Labrador Current and entered the central Labrador Sea.

a. Detection of frontal instabilities around deep convection

Conditions supporting symmetric instability (SI) are investigated at the deep convection boundaries. These include

conditions where PV is negative, which corresponds to both positive stratification ($N^2 > 0$) and also large lateral buoyancy gradients (b_x), as detected by the gradient Richardson number ϕ_{Ri_b}. We also investigate the role of destabilizing atmospheric forcing in setting up conditions for submesoscale instabilities, and check whether the convective layer differs from the MLD.

For example, on 20 and 26 February, sg638 observed both freshwater intrusions and strong lateral buoyancy gradients (suggestive of strong baroclinic flows through thermal wind, Fig. 8c). Within the mixed layer, these large b_x corresponded to slanted isopycnals and weak but stable stratification (Fig. 8b). Both the stronger b_x and the reduced and positive N^2 contribute to
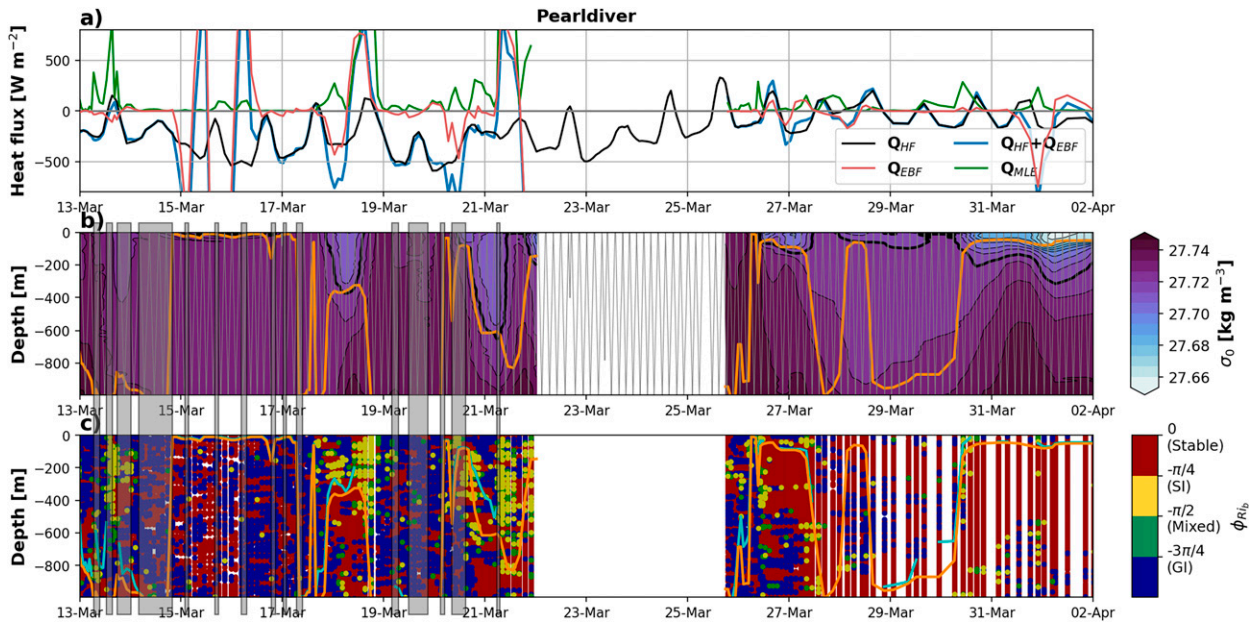
FIG. 9. As in Figs. 8a, 8b, and 8e, but for temporal restratification sampled by Pearldiver.

reducing PV below 0 (Fig. 8d). Separating the contributions to negative PV, we find in this case that $|q_{bc}| > q_{vert}$ with $q_{vert} > 0$, which are conditions suitable for symmetrically unstable flows (documented visually by ϕ_{Ri_b}, yellow dots in Fig. 8e). Additionally, the presence of SI is also suggested at the temporal convection boundary (16–30 March) around freshwater intrusions (Figs. 9b,c), although the presence of gray shading indicates a potential low b_x and an underestimation of SI over this period when the glider traveled to the northeast and the DAC was mainly to the southwest (not shown).

Over the three glider deployments, SI are present during 6.5% of restratifying periods but only 1.1% during convective periods; gravitational instabilities (GI) are present for 26.2% over both convective and restratifying periods. Although the presence of some isolated points (Figs. 8e and 9c) can depend on the choices of decorrelation length scales (L_x and L_z) used in the optimal interpolation, we focus our discussion on clouds of points that are independent on L_x and L_z. Furthermore, using unpumped CT sails for the Seagliders can result in spurious salinity spikes that potentially remain after our postprocessing. This would result in an overestimate of GI. In the present study, we are focusing on SI and so the main results are not affected. Using L_x/L_z of 6 km/25 m and of 10 km/30 m does not significantly change the number of SI during restratifying periods (7.5% and 5.5%, respectively) and during convective periods (1.5% and 0.8%), or the number of GI during both periods (30.9% and 28.1%).

On 20 February, we also have an example where the convective layer depth h (defined in section 2e) was shallower than the mixed layer depth H (Fig. 8e). This condition also supports the presence of symmetrically unstable flows, for $-h > z > -H$ (Taylor and Ferrari 2010). In this layer, the restratifying effect of SI may exceed the destabilizing

surface fluxes. In contrast, within the surface convective layer $z > -h$, we might expect that the destabilizing surface fluxes overpower the restratifying effect of SI. Instances where h is shallower than H by 100–200 m occur in the regions identified as spatial boundaries of the convective region (Fig. 8e) and as convection is transitioning to restratification (temporal change, Fig. 9c). To some extent, the periods where h differs from H correspond to periods where symmetric instability was identified by the gradient Richardson number ϕ_{Ri_b}. One example of this occurred on 20 February between 200 and 400 m (Fig. 8e). In this part of the dataset, PV was negative (Fig. 8d) and vertical stratification was weak but positive (Fig. 8b).

During restratifying periods, remnants of SI (and GI) can persist below the MLD, for example before the 27 February (Fig. 8e). Therefore, fast capping (or shoaling MLD) of recently convected water masses by shallow fronts with large b_x (Fig. 8c) subducts weakly stratified waters. This contrasts with convective periods, characterized by a stable MLD ≈ 700 m (before 19 February in Fig. 8) associated with enhanced stratification (Fig. 8b), low b_x (Fig. 8c), and large PV (Fig. 8d) just below the MLD. SI events are coupled with strong MLD variability (Fig. 8e), however, given the random glider sampling relative to the frontal direction and the transient submesoscale features moving along with gliders, a direct relationship is not maintained for every event. Nevertheless, two SI events sampled by sg602 (not shown) associated with warm intrusions unequivocally connect SI with MLD shoaling by up to ~500 m over several hours (orange line in 11 and 13 February in Fig. 4c). The first event subducts a layer of negative PV and unstable stratification below the MLD, as also seen for example on 20 February around 600–800 m (Fig. 8e). On 19–20 February (Fig. 8b), downward intrusions of relatively

low-density waters (cool and fresh) along with upward intrusions of dense waters (warm and salty) below the MLD around 600 m should characterize subduction of surface properties potentially linked with remnants of SI. Furthermore, SI should be interpreted cautiously below the MLD as they might partly result from lateral density oscillations appearing as spatial aliasing of internal waves in Fig. 8b.

The dependence of MLD on b_x in convective boundaries (Fig. 8c) also suggests the important role of MLE for restratifying the region. MLE occur after the onset of SI, as they persist without requiring a negative PV. This restratifying role is quantified by the buoyancy flux in equivalent heat flux, Q_{MLE}, which by definition is always positive. Strong Q_{MLE} (>500 W m^{-2}) appears both at the convective spatial and temporal boundaries due to deep MLD coupled with large b_x. Approaching the end of convection when Q_{HF} tends to zero, the contribution of Q_{MLE} relative to Q_{HF} increases (Fig. 9a) further accelerating restratification.

b. Destabilizing atmospheric fluxes

The effects of surface heat fluxes and winds on PV are now investigated. Because PV is mostly a conserved quantity outside diffusive and viscous boundary layers (Taylor and Ferrari 2010), surface heat fluxes and winds can predominantly decrease PV toward negative values in the central Labrador Sea (when $B_0 + \text{EBF} > 0$). This PV reduction opposes the restratification by SI (which mixes low-PV surface waters with neighboring high-PV waters) and instead can maintain the conditions for instabilities at frontal flows by maintaining or creating large lateral buoyancy gradients. In the observed glider dataset, the buoyant fresh anomalies (intrusions of freshwater) may be associated with either anomalously cool or warm temperatures (e.g., on 20 and 26 February, respectively, in Fig. 4b). As a result, we cannot directly link surface heat fluxes Q_{HF} with SI. Furthermore, the strong daily variability of the surface heat flux (daily ranges of up to ≈ 200 W m^{-2}) can act against the overall wintertime cooling in the region, and means that the heat forcing over the front is not constant. To establish—over the whole dataset—whether the atmospheric heat flux Q_{HF} affects the frontal strength, we investigate the relationship between Q_{HF} and the vertical and baroclinic components of vorticity (q_{vert} and q_{bc}) in winter (Fig. 10a) and spring (Fig. 10b). Overall we find that larger heat fluxes (Q_{HF}) coincide with sharper fronts (larger amplitude b_x or q_{bc}) in winter, which can be seen as an intensification of the blue color along the lower edge of the colored squares in Fig. 10a. Notably, this pattern of higher buoyancy gradients (larger amplitude q_{bc}) with stronger heat fluxes (dark blue colors) seems to hold down to $q_{bc} = -3 \times 10^{-11}$ s^{-3} for conditions supporting SI, which are identified using the gradient Richardson number as the narrow wedge with positive q_{vert}. Here we find an average $Q_{HF} \approx -300$ W m^{-2} for q_{bc} from -4×10^{-11} to 0 (Fig. 10a). In contrast, there appears to be no clear relationship between Q_{HF} and vertical stratification (q_{vert}). After deep convection (Fig. 10b), average heat fluxes are warming (positive) and there is no apparent relationship between heat fluxes and buoyancy gradients. Since it is unlikely that the heat fluxes are responding to or resulting from the observed horizontal gradients, the pattern found in Fig. 10a suggests that instead the horizontal density gradients are intensified as a result of the stronger destabilizing atmospheric fluxes during deep convection.

We carry out a similar decomposition with Ekman buoyancy fluxes (Q_{EBF}) against horizontal and vertical components of PV in Figs. 10d and 10e rather than surface atmospheric fluxes (Q_{HF}). Downfront (upfront) winds that mix (restratify) the boundary layer are characterized by a negative (positive) Ekman buoyancy forcing in equivalent heat flux, Q_{EBF}. Overall, the amplitude of Q_{EBF} is larger over stronger fronts (larger amplitude q_{bc}) as expected from the dependence of Q_{EBF} on b_x. In March, when surface heat loss abates, $|Q_{EBF}|$ (>500 W m^{-2}) can counteract or reinforce Q_{HF}. For example, on 18 March (Fig. 9a), there is an occurrence of low Q_{HF}, while Q_{EBF} is strongly negative and then positive. From the gradient Richardson calculation, it appears that these conditions contribute to negative PV and might correspond to occurrences of SI (Fig. 9c). Taking the whole dataset together, Fig. 10d shows that there is a set of occurrences of negative Q_{EBF} (blue squares) around $q_{bc} = -3.0 \times 10^{-11}$ s^{-3}.

The ensuing restratifying effect of SI underscores that strong winter atmospheric wind and buoyancy forcing may unexpectedly incite the cessation of deep convection. Alternatively, an opposite Ekman transport can push lighter over denser waters and induces a direct restratification, as quantified by positive Q_{EBF} seen in Fig. 10d and in Fig. 9a. The relationship between b_x and atmospheric forcing (stronger $|b_x|$ when atmospheric forcing is more negative) supports the idea that external forcings may precondition flows to submesoscale instabilities.

5. Restratification by lateral eddy fluxes

Having identified freshwater intrusions that are potentially escaping from the Labrador Current and decaying within the convective region, along with the expected warm intrusions (Gelderloos et al. 2011), the role of freshwater intrusions is now assessed in a large-scale buoyancy budget of the Labrador Sea's interior (Straneo 2006b), and more specifically against the atmospheric buoyancy forcing,

$$\frac{\partial}{\partial t}\int_V \overline{\rho}\, dV + \int_P\int_H \overline{u'\rho'}\, dz\, dl = \frac{\rho_0}{g}\int_A B_0\, dS, \qquad (4)$$

for a convective cylinder of area A, depth H, volume V, and perimeter P assuming a flat-bottom ocean without interior currents. Primes denote deviations from the time mean noted by overlines. Baroclinic instabilities flatten isopycnals of the Labrador Current by bringing buoyant waters toward the interior and dense LSW toward the Labrador Current. This flattening opposes convection that increases lateral density gradients by steepening isopycnals across the Labrador Current. An upper limit of $H = 400$ m characterizes freshwater intrusions (Fig. 8b). In steady state, the lateral eddy buoyancy flux balances the atmospheric buoyancy forcing [last two terms of Eq. (4)]. During a convection–restratification cycle over $\tau = 3.5$ months, equivalent density profiles are found in
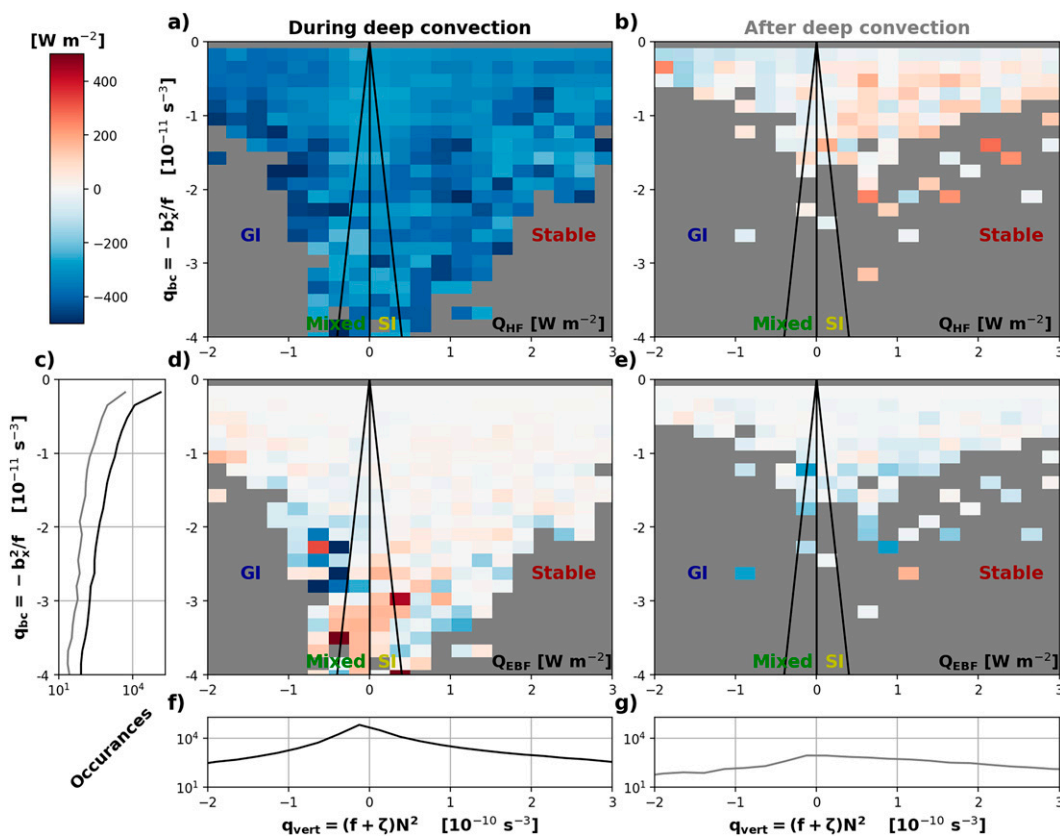
FIG. 10. Median bin-averaged (a),(b) atmospheric heat flux (Q_{HF}) and (d),(e) Ekman heat flux (Q_{EBF}) as a function of the PV vertical (q_{vert}) and baroclinic (q_{bc}) components during the convective period for the three gliders from mid-January until late March in (a) and (d) (red and blue shading in Fig. 4) and after the convective period from April to May in (b) and (e) for Pearldiver only. The occurrences of (c) q_{bc} and (f),(g) q_{vert} during the convective period (black) and after the convective period (gray). The black lines in (a), (b) and (d), (e) separate the regimes where overturning instabilities can arise for negative potential vorticity: gravitational instabilities (GI), mixed regime gravitational/symmetric instabilities (Mixed), symmetric instabilities (SI); and stable conditions (red).

the deep convection region from January to April (Fig. 6c), Eq. (4) becomes with $\Delta\rho \approx 0$

$$\overline{u'\rho'} = \frac{r}{2H}\left(\frac{\rho_0}{g}B_0 - H\frac{\Delta\rho}{\tau}\right) \approx \frac{r\rho_0}{2Hg}B_0. \qquad (5)$$

An estimate of $-(g/\rho_0)\overline{u'\rho'}$ gives 13.1×10^{-6} m² s⁻³ over a convective region of radius $r = 250$ km. In addition, the lateral eddy buoyancy flux is parameterized assuming geostrophic current within the Labrador Current (Spall 2004; Straneo 2006b) with $V_{lc} = gH\delta\rho/(\rho_0 fL)$ and $c = 0.025$ a nondimensional correlation coefficient (Spall 2004)

$$\overline{u'\rho'} = c\delta\rho V_{lc} \approx \frac{cgH\rho_0}{fL}(\beta\delta S_A - \alpha\delta\Theta)^2. \qquad (6)$$

The boundary current width L of 172 km encompasses the Labrador Current along with the transition zone between the deep convection region and the Labrador Current (between 17 February and 4 March in Fig. 8b). Temperature ($\delta\Theta = -0.38°$C) and salinity anomalies ($\delta S_A = -0.42$ g kg⁻¹) across this boundary current

are taken from depth-averaged profiles in the top 400 m at these dates. This shallow estimate $-(g/\rho_0)\overline{u'\rho'}$ gives 4.0×10^{-6} m² s⁻³ due to freshwater intrusions. An equivalent calculation for warm Irminger Waters (400 m < z < 1000 m) gives 0.6×10^{-6} m² s⁻³. The shallow calculation using an interior profile after restratification (end of April, Fig. 6) instead of February, gives 1.1×10^{-6} m² s⁻³ (with $L = 249$ km).

These calculations underline the potential role of the lateral fluxes of shallow freshwater intrusions in the restratification compared with the role of warm deep Irminger Waters. Buoyancy import by freshwater fluxes roughly balances 31% of the surface buoyancy loss and reaches a maximum in winter. This estimate roughly agrees with the findings of Fig. 6 in which a third of the buoyancy gain during restratification was attributed to freshwater intrusions, while the remaining two-thirds might come from warm waters potentially originating in the West Greenland Current. In Fig. 6b, this ratio of buoyancy gain by freshwater intrusions remained unchanged between the restratification's end date (30 March) and the time at which the winter buoyancy loss is fully recovered (28 April). Although Eq. (5) was integrated to 28 April to obtain $\Delta\rho \approx 0$, only 10%

of the lateral buoyancy flux that occurred in late April would be sufficient to restratify and to shallow the deep convection site's MLD to ~50 m in late March (labels of Fig. 6b).

6. Conclusions

Glider deployments in the winter of 2019/20 highlighted the contribution of submesoscale and mesoscale currents to the cessation of the Labrador Sea convection. Freshwater intrusions, plausibly arising from neighboring Labrador Current instabilities, populate the basin interior along with the previously observed warm (Lilly et al. 2003) and freshwater eddies originating further away in the West Greenland Current (Hátún et al. 2007). Using two estimates, these freshwater intrusions contribute a third of the buoyancy necessary to trigger restratification in late March, while the warm intrusions might contribute to the remaining buoyancy. This reasoning is underpinned by the leading role of freshwater intrusions in reducing density both at the convection boundaries, alongside the Labrador Current, but also in the convection core in late winter. In addition, following convection the ML stratifies quickly in salinity and not in temperature.

Our study detected winter freshwater fluxes, previously identified from April only, in the convective region (Schmidt and Send 2007), while ascribing a potential origin for these fluxes. Assuming winter baroclinic instabilities of the Labrador Current, these lateral intrusions balance a third of the local winter atmospheric buoyancy loss. These intrusions appear throughout most of the winter at the convection boundaries, although they appear only two weeks prior to restratification in the convective region, potentially due to their fast decay by submesoscale dynamics of frontal flows.

In mid-January, heat loss to the atmosphere triggers gravitational instabilities and convection. Subsequent to this onset of convection, an upward salinity flux is associated with MLD deepening. Furthermore, at the convection temporal and spatial boundaries, enhanced lateral buoyancy gradients (b_x) coupled with weak stratification sustain submesoscales instabilities. These enhanced frontal flows mostly coincide with fresh and warm intrusions endorsing their restratifying role confirmed by the MLD dependence on b_x. Winter downfront winds and atmospheric cooling participate in generating symmetrically unstable flows, which potentially transform frontal kinetic energy into turbulent mixing. The buoyant intrusions are then mixed with the newly formed dense waters, which triggers restratification.

Altogether, restratification relies on winter atmospheric forcing, which actively contributes to the decay of buoyant intrusions, instead of atmospheric warming. Restratification occurs in winter simultaneously with convection not sequentially. This underscores the importance of sampling, understanding, and parameterizing the processes behind the life cycle of mesoscale and submesoscale dynamics. Eddy shedding and freshwater intrusion depend on topography (Spall 2004), winds, sea ice conditions (Manucharyan and Thompson 2017), and baroclinic instabilities of the Labrador Current (Eden and Böning 2002). Parameterizing these instabilities is necessary to accurately represent the ventilation of LSW in climate models (Yeager et al. 2021) as recently initiated (Pennelly and Myers 2020; Tagklis

et al. 2020), despite a minor restratifying role from freshwater intrusions in both studies. Our results suggest in winter a link between freshwater fluxes of Arctic and Greenland origins—likely to increase in a changing climate—with the Labrador Sea deep convection, fundamental to the export of LSW freshwater, oxygen, and anthropogenic CO_2 to lower latitudes (Koelling et al. 2022).

REFERENCES

Aagaard, K., and E. C. Carmack, 1989: The role of sea ice and other fresh water in the Arctic circulation. *J. Geophys. Res.*, **94**, 14 485–14 498, https://doi.org/10.1029/JC094iC10p14485.

Bachman, S. D., B. Fox-Kemper, J. R. Taylor, and L. N. Thomas, 2017: Parameterization of frontal symmetric instabilities. I:

Theory for resolved fronts. *Ocean Modell.*, **109**, 72–95, https://doi.org/10.1016/j.ocemod.2016.12.003.

Bamber, J., M. van den Broeke, J. Ettema, J. Lenaerts, and E. Rignot, 2012: Recent large increase in freshwater fluxes from Greenland into the North Atlantic. *Geophys. Res. Lett.*, **39**, L19501, https://doi.org/10.1029/2012GL052552.

Bennett, J. S., F. R. Stahr, C. C. Eriksen, M. C. Renken, W. E. Snyder, and L. J. V. Uffelen, 2021: Assessing Seaglider model-based position accuracy on an acoustic tracking range. *J. Atmos. Oceanic Technol.*, **38**, 1111–1123, https://doi.org/10.1175/JTECH-D-20-0091.1.

Böning, C. W., E. Behrens, A. Biastoch, K. Getzlaff, and J. L. Bamber, 2016: Emerging impact of Greenland meltwater on deepwater formation in the North Atlantic Ocean. *Nat. Geosci.*, **9**, 523–527, https://doi.org/10.1038/ngeo2740.

Bosse, A., and I. Fer, 2019: Mean structure and seasonality of the Norwegian Atlantic Front Current along the Mohn Ridge from repeated glider transects. *Geophys. Res. Lett.*, **46**, 13 170–13 179, https://doi.org/10.1029/2019GL084723.

——, P. Testor, P. Damien, C. Estournel, P. Marsaleix, L. Mortier, L. Prieur, and V. Taillandier, 2021: Wind-forced submesoscale symmetric instability around deep convection in the northwestern Mediterranean Sea. *Fluids*, **6**, 123, https://doi.org/10.3390/fluids6030123.

Brandt, P., F. A. Schott, A. Funk, and C. S. Martins, 2004: Seasonal to interannual variability of the eddy field in the Labrador Sea from satellite altimetry. *J. Geophys. Res.*, **109**, C02028, https://doi.org/10.1029/2002JC001551.

Cavalieri, D., C. Parkinson, P. Gloersen, and H. Zwally, 1996: Sea ice concentrations from Nimbus-7 SMMR and DMSP SSM/I-SSMIS passive microwave data, version 1. National Snow and Ice Data Center, accessed 2 February 2021, https://doi.org/10.5067/8GQ8LZQVL0VL.

Chanut, J., B. Barnier, W. Large, L. Debreu, T. Penduff, J. M. Molines, and P. Mathiot, 2008: Mesoscale eddies in the Labrador Sea and their contribution to convection and restratification. *J. Phys. Oceanogr.*, **38**, 1617–1643, https://doi.org/10.1175/2008JPO3485.1.

Chin, T. M., J. Vazquez-Cuervo, and E. M. Armstrong, 2017: A multi-scale high-resolution analysis of global sea surface temperature. *Remote Sens. Environ.*, **200**, 154–169, https://doi.org/10.1016/j.rse.2017.07.029.

Cuny, J., P. B. Rhines, P. P. Niiler, and S. Bacon, 2002: Labrador Sea boundary currents and the fate of the Irminger Sea water. *J. Phys. Oceanogr.*, **32**, 627–647, https://doi.org/10.1175/1520-0485(2002)032<0627:LSBCAT>2.0.CO;2.

——, ——, F. Schott, and J. Lazier, 2005: Convection above the Labrador continental slope. *J. Phys. Oceanogr.*, **35**, 489–511, https://doi.org/10.1175/JPO2700.1.

Dickson, R. R., J. Meincke, S.-A. Malmberg, and A. J. Lee, 1988: The "great salinity anomaly" in the northern North Atlantic 1968–1982. *Prog. Oceanogr.*, **20**, 103–151, https://doi.org/10.1016/0079-6611(88)90049-3.

——, J. Lazier, J. Meinke, P. Rhines, and J. Swift, 1996: Long-term coordinated changes in the convective activity of the North Atlantic. *Prog. Oceanogr.*, **38**, 241–295, https://doi.org/10.1016/S0079-6611(97)00002-5.

Dukhovskoy, D. S., I. Yashayaev, A. Proshutinsky, J. L. Bamber, I. L. Bashmachnikov, E. P. Chassignet, C. M. Lee, and A. J. Tedstone, 2019: Role of Greenland freshwater anomaly in the recent freshening of the subpolar North Atlantic. *J. Geophys. Res. Oceans*, **124**, 3333–3360, https://doi.org/10.1029/2018JC014686.

du Plessis, M., S. Swart, I. J. Ansorge, A. Mahadevan, and A. F. Thompson, 2019: Southern Ocean seasonal restratification delayed by submesoscale wind–front interactions. *J. Phys. Oceanogr.*, **49**, 1035–1053, https://doi.org/10.1175/JPO-D-18-0136.1.

Eden, C., and C. Böning, 2002: Sources of eddy kinetic energy in the Labrador Sea. *J. Phys. Oceanogr.*, **32**, 3346–3363, https://doi.org/10.1175/1520-0485(2002)032<3346:SOEKEI>2.0.CO;2.

Eriksen, C. C., T. J. Osse, R. D. Light, T. Wen, T. W. Lehman, P. L. Sabin, J. W. Ballard, and A. M. Chiodi, 2001: Seaglider: A long-range autonomous underwater vehicle for oceanographic research. *IEEE J. Oceanic Eng.*, **26**, 424–436, https://doi.org/10.1109/48.972073.

Florindo-López, C., S. Bacon, Y. Aksenov, L. Chafik, E. Colbourne, and N. P. Holliday, 2020: Arctic Ocean and Hudson Bay freshwater exports: New estimates from seven decades of hydrographic surveys on the Labrador Shelf. *J. Climate*, **33**, 8849–8868, https://doi.org/10.1175/JCLI-D-19-0083.1.

Fox-Kemper, B., R. Ferrari, and R. Hallberg, 2008: Parameterization of mixed layer eddies. Part I: Theory and diagnosis. *J. Phys. Oceanogr.*, **38**, 1145–1165, https://doi.org/10.1175/2007JPO3792.1.

Frajka-Williams, E., P. B. Rhines, and C. C. Eriksen, 2014: Horizontal stratification during deep convection in the Labrador Sea. *J. Phys. Oceanogr.*, **44**, 220–228, https://doi.org/10.1175/JPO-D-13-069.1.

Gascard, J. C., and R. A. Clarke, 1983: The formation of Labrador Sea Water. Part II: Mesoscale and smaller-scale processes. *J. Phys. Oceanogr.*, **13**, 1779–1797, https://doi.org/10.1175/1520-0485(1983)013<1779:TFOLSW>2.0.CO;2.

Gelderloos, R., C. A. Katsman, and S. S. Drijfhout, 2011: Assessing the roles of three eddy types in restratifying the Labrador Sea after deep convection. *J. Phys. Oceanogr.*, **41**, 2102–2119, https://doi.org/10.1175/JPO-D-11-054.1.

——, F. Straneo, and C. A. Katsman, 2012: Mechanisms behind the temporary shutdown of deep convection in the Labrador Sea: Lessons from the great salinity anomaly years 1968–71. *J. Climate*, **25**, 6743–6755, https://doi.org/10.1175/JCLI-D-11-00549.1.

Gula, J., J. Taylor, A. Shcherbina, and A. Mahadevan, 2021: *Submesoscale Processes and Mixing.* Elsevier, 384 pp.

Haine, T. W. N., and J. Marshall, 1998: Gravitational, symmetric, and baroclinic instability of the ocean mixed layer. *J. Phys. Oceanogr.*, **28**, 634–658, https://doi.org/10.1175/1520-0485(1998)028<0634:GSABIO>2.0.CO;2.

Hátún, H., C. C. Eriksen, and P. B. Rhines, 2007: Buoyant eddies entering the Labrador Sea observed with gliders and altimetry. *J. Phys. Oceanogr.*, **37**, 2838–2854, https://doi.org/10.1175/2007JPO3567.1.

Hersbach, H., and Coauthors, 2020: The ERA5 global reanalysis. *Quart. J. Roy. Meteor. Soc.*, **146**, 1999–2049, https://doi.org/10.1002/qj.3803.

Heuzé, C., 2017: North Atlantic deep water formation and AMOC in CMIP5 models. *Ocean Sci.*, **13**, 609–622, https://doi.org/10.5194/os-13-609-2017.

Hosegood, P., M. C. Gregg, and M. H. Alford, 2006: Submesoscale lateral density structure in the oceanic surface mixed layer. *Geophys. Res. Lett.*, **33**, L22604, https://doi.org/10.1029/2006GL026797.

Hoskins, B. J., 1974: The role of potential vorticity in symmetric stability and instability. *Quart. J. Roy. Meteor. Soc.*, **100**, 480–482, https://doi.org/10.1002/qj.49710042520.

Hurrell, J., 2022: Hurrell North Atlantic Oscillation (NAO) Index (PC-based). NCAR, accessed 12 January 2022,

https://climatedataguide.ucar.edu/climate-data/hurrell-north-atlantic-oscillation-nao-index-pc-based.

Jones, H., and J. Marshall, 1993: Convection with rotation in a neutral ocean: A study of open-ocean deep convection. *J. Phys. Oceanogr.*, **23**, 1009–1039, https://doi.org/10.1175/1520-0485(1993)023%3C1009:CWRIAN%3E2.0.CO;2.

——, and ——, 1997: Restratification after deep convection. *J. Phys. Oceanogr.*, **27**, 2276–2287, https://doi.org/10.1175/1520-0485(1997)027<2276:RADC>2.0.CO;2.

Katsman, C. A., M. A. Spall, and R. S. Pickart, 2004: Boundary current eddies and their role in the restratification of the Labrador Sea. *J. Phys. Oceanogr.*, **34**, 1967–1983, https://doi.org/10.1175/1520-0485(2004)034<1967:BCEATR>2.0.CO;2.

Koelling, J., D. Atamanchuk, J. Karstensen, P. Handmann, and D. W. R. Wallace, 2022: Oxygen export to the deep ocean following Labrador Sea Water formation. *Biogeosciences*, **19**, 437–454, https://doi.org/10.5194/bg-19-437-2022.

Koenigk, T., and Coauthors, 2021: Deep mixed ocean volume in the Labrador Sea in HighResMIP models. *Climate Dyn.*, **57**, 1895–1918, https://doi.org/10.1007/s00382-021-05785-x.

Lab Sea Group, 1998: The Labrador Sea deep convection experiment. *Bull. Amer. Meteor. Soc.*, **79**, 2033–2058, https://doi.org/10.1175/1520-0477(1998)079<2033:TLSDCE>2.0.CO;2.

Large, W. G., J. C. McWilliams, and S. C. Doney, 1994: Oceanic vertical mixing: A review and a model with a nonlocal boundary layer parameterization. *Rev. Geophys.*, **32**, 363–403, https://doi.org/10.1029/94RG01872.

Lazier, J. R. N., 1973: The renewal of Labrador Sea Water. *Deep-Sea Res. Oceanogr. Abstr.*, **20**, 341–353, https://doi.org/10.1016/0011-7471(73)90058-2.

——, 1980: Oceanographic conditions at Ocean Weather Ship Bravo, 1964–1974. *Atmos.–Ocean*, **18**, 227–238, https://doi.org/10.1080/07055900.1980.9649089.

——, R. Hendry, A. Clarke, I. Yashayaev, and P. Rhines, 2002: Convection and restratification in the Labrador Sea, 1990–2000. *Deep-Sea Res. I*, **49**, 1819–1835, https://doi.org/10.1016/S0967-0637(02)00064-X.

Le Bras, I. A.-A., J. Callies, F. Straneo, T. C. Biló, J. Holte, and H. L. Johnson, 2022: Slantwise convection in the Irminger Sea. *J. Geophys. Res. Oceans*, **127**, e2022JC019071, https://doi.org/10.1029/2022JC019071.

Lilly, J. M., P. B. Rhines, F. Schott, K. Lavender, J. Lazier, U. Send, and E. D'Asaro, 2003: Observations of the Labrador Sea eddy field. *Prog. Oceanogr.*, **59**, 75–176, https://doi.org/10.1016/j.pocean.2003.08.013.

Lozier, M. S., and Coauthors, 2019: A sea change in our view of overturning in the subpolar North Atlantic. *Science*, **363**, 516–521, https://doi.org/10.1126/science.aau6592.

Lumpkin, R., and L. Centurioni, 2019: NOAA global drifter program quality-controlled 6-hour interpolated data from ocean surface drifting buoys. NOAA National Centers for Environmental Information, accessed 21 November 2022, https://doi.org/10.25921/7ntx-z961.

Mahadevan, A., E. D'Asaro, C. Lee, and M. J. Perry, 2012: Eddy-driven stratification initiates North Atlantic spring phytoplankton blooms. *Science*, **337**, 54–58, https://doi.org/10.1126/science.1218740.

Manabe, S., and R. J. Stouffer, 1995: Simulation of abrupt climate change induced by freshwater input to the North Atlantic Ocean. *Nature*, **378**, 165–167, https://doi.org/10.1038/378165a0.

Manucharyan, G. E., and A. F. Thompson, 2017: Submesoscale sea ice-ocean interactions in marginal ice zones. *J. Geophys. Res. Oceans*, **122**, 9455–9475, https://doi.org/10.1002/2017JC012895.

Marshall, J., and F. Schott, 1999: Open-ocean convection: Observations, theory and models. *Rev. Geophys.*, **37**, 1–64, https://doi.org/10.1029/98RG02739.

Maxworthy, T., and S. Narimousa, 1994: Unsteady, turbulent convection into a homogeneous, rotating fluid, with oceanographic applications. *J. Phys. Oceanogr.*, **24**, 865–887, https://doi.org/10.1175/1520-0485(1994)024%3C0865:UTCIAH%3E2.0.CO;2.

McGeehan, I., and W. Maslowski, 2011: Impact of shelf-basin freshwater transport on deep convection in the western Labrador Sea. *J. Phys. Oceanogr.*, **41**, 2187–2210, https://doi.org/10.1175/JPO-D-11-01.1.

Morrow, R., and Coauthors, 2019: Global observations of fine-scale ocean surface topography with the Surface Water and Ocean Topography (SWOT) mission. *Front. Mar. Sci.*, **6**, 232, https://doi.org/10.3389/fmars.2019.00232.

Myers, P. G., 2005: Impact of freshwater from the Canadian Arctic Archipelago on the Labrador Sea water formation. *Geophys. Res. Lett.*, **32**, L06605, https://doi.org/10.1029/2004GL022082.

Pennelly, C., and P. G. Myers, 2020: Introducing LAB60: A 1/60° NEMO 3.6 numerical simulation of the Labrador Sea. *Geosci. Model Dev.*, **13**, 4959–4975, https://doi.org/10.5194/gmd-13-4959-2020.

——, X. Hu, and P. G. Myers, 2019: Cross-isobath freshwater exchange within the North Atlantic subpolar gyre. *J. Geophys. Res. Oceans*, **124**, 6831–6853, https://doi.org/10.1029/2019JC015144.

Pickart, R. S., D. J. Torres, and R. A. Clarke, 2002: Hydrography of the Labrador Sea during convection. *J. Phys. Oceanogr.*, **32**, 428–457, https://doi.org/10.1175/1520-0485(2002)032<0428:HOTLSD>2.0.CO;2.

Proshutinsky, A., and Coauthors, 2019: Analysis of the Beaufort Gyre freshwater content in 2003–2018. *J. Geophys. Res. Oceans*, **124**, 9658–9689, https://doi.org/10.1029/2019JC015281.

Rahmstorf, S., 1995: Bifurcations of the Atlantic thermohaline circulation in response to changes in the hydrological cycle. *Nature*, **378**, 145–149, https://doi.org/10.1038/378145a0.

Rhein, M., and Coauthors, 2002: Labrador Sea water: Pathways, CFC inventory, and formation rates. *J. Phys. Oceanogr.*, **32**, 648–665, https://doi.org/10.1175/1520-0485(2002)032<0648:LSWPCI>2.0.CO;2.

Roemmich, D., and J. Gilson, 2009: The 2004–2008 mean and annual cycle of temperature, salinity, and steric height in the global ocean from the Argo Program. *Prog. Oceanogr.*, **82**, 81–100, https://doi.org/10.1016/j.pocean.2009.03.004.

Rykova, T., F. Straneo, J. Lilly, and I. M. Yashayaev, 2009: Irminger Current anticyclones in the Labrador Sea observed in the hydrographic record, 1990–2004. *J. Mar. Res.*, **67**, 361–384, https://doi.org/10.1357/002224009789954739.

Sabine, C. L., and Coauthors, 2004: The oceanic sink for anthropogenic CO_2. *Science*, **305**, 367–371, https://doi.org/10.1126/science.1097403.

Sathiyamoorthy, S., and G. W. K. Moore, 2002: Buoyancy flux at ocean weather station Bravo. *J. Phys. Oceanogr.*, **32**, 458–474, https://doi.org/10.1175/1520-0485(2002)032<0458:BFAOWS>2.0.CO;2.

Schmidt, S., and U. Send, 2007: Origin and composition of seasonal Labrador Sea freshwater. *J. Phys. Oceanogr.*, **37**, 1445–1454, https://doi.org/10.1175/JPO3065.1.

Spall, M. A., 2004: Boundary currents and watermass transformation in marginal seas. *J. Phys. Oceanogr.*, **34**, 1197–1213, https://doi.org/10.1175/1520-0485(2004)034<1197:BCAWTI>2.0.CO;2.

Steffen, E. L., and E. A. D'Asaro, 2004: Meso- and submesoscale structure of a convecting field. *J. Phys. Oceanogr.*, **34**, 44–60,

https://doi.org/10.1175/1520-0485(2004)034<0044:MASSOA>2.0.CO;2.

Straneo, F., 2006a: Heat and freshwater transport through the central Labrador Sea. *J. Phys. Oceanogr.*, **36**, 606–628, https://doi.org/10.1175/JPO2875.1.

——, 2006b: On the connection between dense water formation, overturning, and poleward heat transport in a convective basin. *J. Phys. Oceanogr.*, **36**, 1822–1840, https://doi.org/10.1175/JPO2932.1.

——, M. Kawase, and S. Riser, 2002: Idealized models of slantwise convection in a baroclinic flow. *J. Phys. Oceanogr.*, **32**, 558–572, https://doi.org/10.1175/1520-0485(2002)032<0558:IMOSCI>2.0.CO;2.

Swingedouw, D., M.-N. Houssais, C. Herbaut, A.-C. Blaizot, M. Devilliers, and J. Deshayes, 2022: AMOC recent and future trends: A crucial role for oceanic resolution and Greenland melting? *Front. Climate*, **4**, 838310, https://doi.org/10.3389/fclim.2022.838310.

Tagklis, F., A. Bracco, T. Ito, and R. M. Castelao, 2020: Submesoscale modulation of deep water formation in the Labrador Sea. *Sci. Rep.*, **10**, 17489, https://doi.org/10.1038/s41598-020-74345-w.

Taylor, J. R., and R. Ferrari, 2009: On the equilibration of a symmetrically unstable front via a secondary shear instability. *J. Fluid Mech.*, **622**, 103–113, https://doi.org/10.1017/S0022112008005272.

——, and ——, 2010: Buoyancy and wind-driven convection at mixed layer density fronts. *J. Phys. Oceanogr.*, **40**, 1222–1242, https://doi.org/10.1175/2010JPO4365.1.

Thomas, L. N., 2005: Destruction of potential vorticity by winds. *J. Phys. Oceanogr.*, **35**, 2457–2466, https://doi.org/10.1175/JPO2830.1.

——, A. Tandon, and A. Mahadevan, 2008: Submesoscale processes and dynamics. *Ocean Modeling in an Eddying Regime*, Geophys. Monogr., Vol. 177, Amer. Geophys. Union, 17–38, https://doi.org/10.1029/177GM04.

——, J. R. Taylor, R. Ferrari, and T. M. Joyce, 2013: Symmetric instability in the Gulf Stream. *Deep-Sea Res. II*, **91**, 96–110, https://doi.org/10.1016/j.dsr2.2013.02.025.

Thomas, M. D., A.-M. Treguier, B. Blanke, J. Deshayes, and A. Voldoire, 2015: A Lagrangian method to isolate the impacts of mixed layer subduction on the meridional overturning circulation in a numerical model. *J. Climate*, **28**, 7503–7517, https://doi.org/10.1175/JCLI-D-14-00631.1.

Thompson, A. F., A. Lazar, C. Buckingham, A. C. Naveira Garabato, G. M. Damerell, and K. J. Heywood, 2016: Open-ocean submesoscale motions: A full seasonal cycle of mixed layer instabilities from gliders. *J. Phys. Oceanogr.*, **46**, 1285–1307, https://doi.org/10.1175/JPO-D-15-0170.1.

Todd, R. E., W. B. Owens, and D. L. Rudnick, 2016: Potential vorticity structure in the North Atlantic western boundary current from underwater glider observations. *J. Phys. Oceanogr.*, **46**, 327–348, https://doi.org/10.1175/JPO-D-15-0112.1.

Vellinga, M., and R. A. Wood, 2002: Global climatic impacts of a collapse of the Atlantic thermohaline circulation. *Climatic Change*, **54**, 251–267, https://doi.org/10.1023/A:1016168827653.

Viglione, G. A., A. F. Thompson, M. M. Flexas, J. Sprintall, and S. Swart, 2018: Abrupt transitions in submesoscale structure in southern Drake Passage: Glider observations and model results. *J. Phys. Oceanogr.*, **48**, 2011–2027, https://doi.org/10.1175/JPO-D-17-0192.1.

Visbeck, M., J. Marshall, and H. Jones, 1996: Dynamics of isolated convective regions in the ocean. *J. Phys. Oceanogr.*, **26**, 1721–1734, https://doi.org/10.1175/1520-0485(1996)026<1721:DOICRI>2.0.CO;2.

Yashayaev, I., and J. W. Loder, 2016: Recurrent replenishment of Labrador Sea Water and associated decadal-scale variability. *J. Geophys. Res. Oceans*, **121**, 8095–8114, https://doi.org/10.1002/2016JC012046.

——, M. Bersch, and H. M. van Aken, 2007: Spreading of the Labrador Sea Water to the Irminger and Iceland basins. *Geophys. Res. Lett.*, **34**, L10602, https://doi.org/10.1029/2006GL028999.

——, I. Peterson, and Z. Wang, 2020: Meteorological, sea ice and physical oceanographic conditions in the Labrador Sea during 2020. DFO Canadian Science Advisory Secretariat, NAFO SCR Doc. 21/037, 45 pp., https://www.nafo.int/Portals/0/PDFs/sc/2021/scr21-037.pdf.

Yeager, S., and Coauthors, 2021: An outsized role for the Labrador Sea in the multidecadal variability of the Atlantic overturning circulation. *Sci. Adv.*, **7**, eabh3592, https://doi.org/10.1126/sciadv.abh3592.

Yu, X., A. C. Naveira Garabato, A. P. Martin, D. G. Evans, and Z. Su, 2019: Wind-forced symmetric instability at a transient mid-ocean front. *Geophys. Res. Lett.*, **46**, 11281–11291, https://doi.org/10.1029/2019GL084309.

Zhang, J., W. Weijer, M. Steele, W. Cheng, T. Verma, and M. Veneziani, 2021: Labrador Sea freshening linked to Beaufort Gyre freshwater release. *Nat. Commun.*, **12**, 1229, https://doi.org/10.1038/s41467-021-21470-3.